Springer

Acta Mechanica Sinica

CrossMark click for updates

• RESEARCH PAPER •

Acta Mech. Sin., Vol. 40, 423345 (2024)
https://doi.org/10.1007/s10409-023-23345-x

Improvements of cohesive zone model on artificial compliance and discontinuous force

Ala Tabiei*, and Li Meng

Department of Mechanical and Materials Engineering, University of Cincinnati, Cincinnati OH 45221-0070, USA

Received September 15, 2023; accepted October 31, 2023; published online June 19, 2024

The cohesive zone model (CZM) has been used widely and successfully in fracture propagation, but some basic problems are still to be solved. In this paper, artificial compliance and discontinuous force in CZM are investigated. First, theories about the cohesive element (local coordinate system, stiffness matrix, and internal nodal force) are presented. The local coordinate system is defined to obtain local separation; the stiffness matrix for an eight-node cohesive element is derived from the calculation of strain energy; internal nodal force between the cohesive element and bulk element is obtained from the principle of virtual work. Second, the reason for artificial compliance is explained by the effective stiffnesses of zero-thickness and finite-thickness cohesive elements. Based on the effective stiffness, artificial compliance can be completely removed by adjusting the stiffness of the finite-thickness cohesive element. This conclusion is verified from 1D and 3D simulations. Third, three damage evolution methods (monotonically increasing effective separation, damage factor, and both effective separation and damage factor) are analyzed. Under constant unloading and reloading conditions, the monotonically increasing damage factor method without discontinuous force and healing effect is a better choice than the other two methods. The proposed improvements are coded in LS-DYNA user-defined material, and a drop weight tear test verifies the improvements.

Cohesive zone model, Stiffness matrix, Artificial compliance, Damage evolution method, Discontinuous force

Citation: A. Tabiei, and L. Meng, Improvements of cohesive zone model on artificial compliance and discontinuous force, Acta Mech. Sin. 40, 423345 (2024), https://doi.org/10.1007/s10409-023-23345-x

1. Introduction

In the past few decades, the cohesive zone model (CZM) has been used extensively in studying fracture propagation, where the cohesive element is used for modeling cohesive interface between edges of shell elements, faces of shell elements, and faces of solid elements, typically for treating delamination. CZM is based on the cohesive zone concept proposed by Barenblatt [1] and Dugdale [2]. It is assumed that at the ahead of the crack tip, there is a thin layer separating two solids in which damage mechanisms leading to the crack are localized, and the behavior of this crack process zone is characterized by traction-separation law called cohesive law. Commonly used cohesive laws include bilinear cohesive law [3], trapezoidal cohesive law [4], polynomial cohesive law [5], and exponential cohesive law [6]. For all these cohesive laws, bilinear cohesive law has become a big part of them. The major advantage of bilinear cohesive law is that a very simple traction-separation law provides results good enough to model with accuracy delamination and cracking [7]. In this paper, bilinear cohesive law is used to investigate artificial compliance and discontinuous force, but the proposed methods can be applied to other displacement-based cohesive laws as well. For a comprehensive understanding of this topic, it is worth mentioning that the piecewise-linear generalizable cohesive element (not assuming a specific cohesive law shape) [8] and some other potential-based or energy-based CZM are also under active investigation [9].

Instead of dealing with stress-strain relation, cohesive law deals with traction-separation or stress-separation relation. The theories about CZM have been studied by many researchers. Yamaguchi et al. [10] used quadratic separation

*Corresponding author. E-mail address: tabieia@ucmail.uc.edu (Ala Tabiei)
Executive Editor: Xiaoding Wei

© The Chinese Society of Theoretical and Applied Mechanics and Springer-Verlag GmbH Germany, part of Springer Nature 2024

criterion to define a damage factor that is used in constitutive matrix and stiffness matrix. Kumar et al. [11] elaborated the quadratic stress criterion for the initiation of damage and the Benzeggagh-Kenane law for the failure of damage evolution in bilinear cohesive law. Sarrado et al. [12] decoupled stiffness into a zero-thickness cohesive element and a linear elastic bulk element to model the strengthening, softening, and failure of finite-thickness adhesive. Trawiński et al. [13,14] investigated 2D and 3D simulations of concrete fracture, and diagonal matrices with only two and three stiffness parameters are regarded as stiffness matrix, which should only be constitutive matrix. Park and Paulino [15] derived a stiffness matrix for a potential-based CZM. Rahul-Kumar et al. [16] derived rate-independent and rate-dependent cohesive laws, and a Jacobian matrix is obtained for the relation between incremental traction and incremental separation. Bak et al. [17] elaborated local coordinate system used in cohesive element, and the tangent constitutive matrix is derived for the incremental traction and incremental separation. Before the initiation of damage or in the linear elastic range, the derivation of the stiffness matrix is straightforward, but because of the nonlinearity of constitutive law after the initiation of damage, a tangent stiffness matrix is needed.

Artificial compliance is a common numerical problem inherent in intrinsic cohesive law, and many methods have been proposed to try to solve it. Tabiei and Meng [18] found that zero-thickness cohesive element with finite stiffness introduces artificial compliance in a PMMA plate tensile test, which would affect the velocity of fracture propagation. Song et al. [19] used a potential-based exponential cohesive law to simulate the fracture of asphalt concrete, and an initial linear-elastic range with an adjustable initial slope is used to reduce artificial compliance. Similarly, Blal et al. [20] summarized some semi-empirical criteria to solve artificial compliance, and the main idea is that the ratio between cohesive element stiffness and bulk element stiffness should be larger than a specific number. Even though much research has been done in this direction, artificial compliance can only be reduced for bilinear cohesive law in many publications, not completely removed, and the delay of stress wave response would be worse if a simulation is time-sensitive. In this paper, we will show that a finite-thickness cohesive element could be an option to solve this problem. On the other hand, there are some other ways to solve this problem. By using the discontinuous Galerkin method, Nguyen [21] proposed a hybrid discontinuous Galerkin/CZM method, where the cohesive element is placed at element faces and artificial compliance is removed by discontinuous Galerkin formulation.

The damage factor for bilinear cohesive law has been well defined, but there is still one thing that can make the damage evolution process different. It is whether current effective separation is its maximum history value or not, and, with it, it leads to two common damage evolution methods, the monotonically increasing effective separation method and the monotonically increasing damage factor method. These two methods are widely and interchangeably used in current research, probably because their difference is not well recognized in publications. Tabiei and Zhang [22,23] investigated monotonically increasing effective separation method on exponential cohesive law, and discontinuous force is found when constant unloading and reloading is used with this effective separation method. To solve this discontinuous force, linear interpolation is used to get traction at each time step based on the current mixed mode ratio. Because this discontinuous force is related to the change of mixed mode ratio, which is hard to control in a simulation, this discontinuous force will be only explained in detail from the traction response analysis of a single cohesive element. But it is important to point this out, and more investigation of this discontinuous force is needed. Instead of using the common damage factor, Tomar et al. [24] used quadratic separation law to get a state variable in the derivation of potential-based bilinear cohesive law. Similarly, Kozinov et al. [25] used normalized effective traction and separation in monotonic mechanical traction-separation law, and the mixed mode ratio is not explicitly shown in the damage factor, so it could avoid the discontinuous force when the mixed mode ratio changes. Park and Paulino [26] presented a comprehensive review of traction-separation law, including potential-based models and displacement-based models.

Another problem with the monotonically increasing effective separation method is that unreasonable failure can happen if the maximum separation in Mode I and Mode II is different. When the load of the cohesive element moves to a mixed mode ratio that has an allowable effective separation less than the maximum history effective separation, the cohesive element would just fail. This means that cohesive elements could fail only because of a change of mixed mode ratio, especially in mixed mode situations. Even in the last several years, monotonically increasing effective separation method is still often used in papers. Gao et al. [27] used intrinsic bilinear cohesive law with a monotonically increasing effective separation method to simulate the impact failure of laminated glass. Hirsch and Kästner [28] used a monotonically increasing effective separation method to simulate adhesive and cohesive failure under microscale conditions. The good thing is that there is no discontinuous force during this unreasonable failure process, which might be the reason why it is used interchangeably with the monotonically increasing damage factor method. Turon et al. [29-31] proposed a relation between the interlaminar strengths to ensure that the predictions obtained using cohesive finite elements are correct for mixed-mode loading

conditions. de Oliveira and Donadon [32] showed that a constant fraction between the damage onset and damage failure would not introduce errors in displacement and energy response. Considering the possible problems with the damage evolution method mentioned above, it should be selected with great caution.

In this paper, improvements of CZM on artificial compliance and discontinuous force are proposed. This paper is constructed as follows. In Sect. 2.1, the local coordinate system is defined to obtain local separation. In Sect. 2.2, stiffness matrix for an eight-node cohesive element is derived from the calculation of strain energy. In Sect. 2.3, the internal nodal force between the cohesive element and bulk element is obtained from the principle of virtual work. In Sect. 3, the reason for artificial compliance is explained by the effective stiffnesses of zero-thickness and finite-thickness cohesive elements. Based on effective stiffness, artificial compliance can be completely removed by adjusting the stiffness of finite-thickness cohesive elements. This conclusion is verified from 1D and 3D simulations. In Sect. 4, three damage evolution methods (monotonically increasing effective separation, damage factor, and both effective separation and damage factor) are analyzed. Under constant unloading and reloading conditions, the monotonically increasing damage factor method without discontinuous force and healing effect is a better choice than the other two methods. In Sect. 5, the proposed improvements are coded in LS-DYNA user-defined material, and a drop weight tear test verifies the improvements. In Sect. 6, conclusions are made.

2. Theories of cohesive element

2.1 Local coordinate system

The cohesive element between the faces of eight-node solid elements is investigated here, as shown in Fig. 1(a). Instead of the stress-strain relation in bulk element, cohesive law deals with traction-separation or stress-separation relation. To get the local stress in the cohesive element, the local separation $\mathbf{s}_l$ between the top and bottom faces of the cohesive element is obtained from global displacement $\mathbf{u}_t$ and $\mathbf{u}_b$, as shown in Eq. (1), where $\mathbf{Q}$ is the coordinate system transformation matrix from global to local coordinate system; $\mathbf{s}_l^0$ is the initial local separation (or thickness of cohesive element) in case of finite-thickness cohesive element is used. $\mathbf{u}_t$ and $\mathbf{u}_b$ can be expressed as shape function N_i ($i = 1, 2, 3, 4$) and node displacement $\mathbf{u}_{ti}$ and $\mathbf{u}_{bi}$ on top and bottom faces. Because local separation is only related to the top and bottom faces, the shape function used here is a function of two local isoparametric element variables ξ and η. This can be obtained by setting the third variable $\varsigma = \pm 1$ for the shape function of a common eight-node solid element, as shown in Eqs. (2) and (3). Note that if a subscript appears twice in the same term, then summation over that subscript is implied in this paper.

$$\mathbf{s}_l = \mathbf{Q}(\mathbf{u}_t - \mathbf{u}_b) - \mathbf{s}_l^0, \tag{1}$$

$$\begin{cases} \mathbf{u}_t = N_i(\xi, \eta)\mathbf{u}_{ti}, & i = 1, 2, 3, 4, \\ \mathbf{u}_b = N_i(\xi, \eta)\mathbf{u}_{bi}, & i = 1, 2, 3, 4, \end{cases} \tag{2}$$

$$\begin{cases} N_i(\xi, \eta) = \dfrac{1}{4}(1 + \xi_i^*\xi)(1 + \eta_i^*\eta), & i = 1, 2, 3, 4, \\ \boldsymbol{\xi}^* = [1, 1, -1, -1], \\ \boldsymbol{\eta}^* = [-1, 1, 1, -1]. \end{cases} \tag{3}$$

To get the $\mathbf{Q}$ in Eq. (1), middle nodes between the top and bottom faces are calculated first, as shown in Eq. (4). Unit vectors, $\mathbf{e}_1$ and $\mathbf{e}_2$, are obtained from middle nodes $\mathbf{x}_{m3}$, $\mathbf{x}_{m1}$ and $\mathbf{x}_{m4}$, $\mathbf{x}_{m2}$, respectively, as shown in Eq. (5) and Fig. 1(b). The direction of x axis ($\mathbf{q}_1$) in the local coordinate system is the opposite of the sum of $\mathbf{e}_1$ and $\mathbf{e}_2$; the direction of y axis ($\mathbf{q}_2$) in the local coordinate system is the same as the difference between $\mathbf{e}_1$ and $\mathbf{e}_2$; the direction of z axis ($\mathbf{q}_3$) in the local coordinate system is the cross product of $\mathbf{q}_1$ and $\mathbf{q}_2$, as shown in Eq. (6) and Fig. 1(c). Since $\mathbf{e}_1$ and $\mathbf{e}_2$ are unit

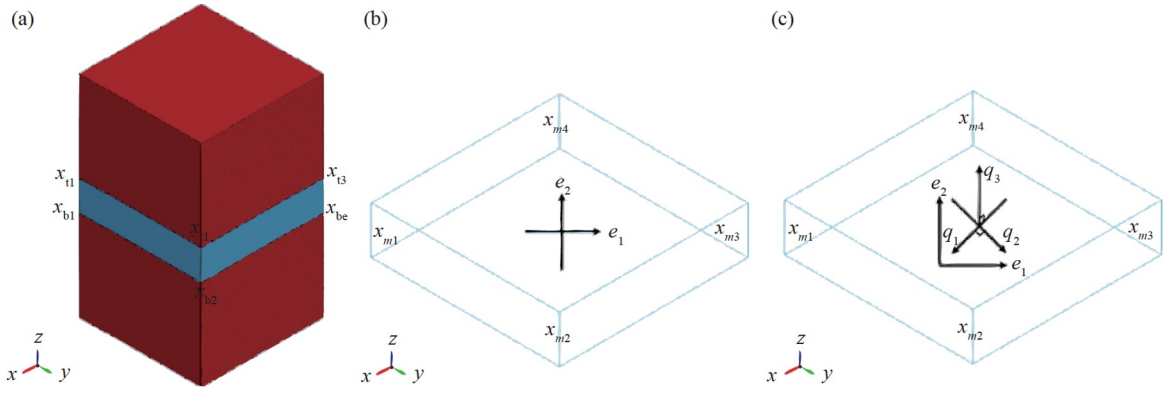

Figure 1 Schematic of the cohesive element. (a) Cohesive element between faces of eight-node solid elements; (b) unit vectors obtained from middle nodes; (c) local coordinate system $\{\mathbf{q}_1, \mathbf{q}_2, \mathbf{q}_3\}$.

vectors, $\mathbf{q}_1$ and $\mathbf{q}_2$ are perpendicular to each other (diagonals of a rhombus are perpendicular to each other).

$$\mathbf{x}_{mi} = \frac{\mathbf{x}_{ti} + \mathbf{x}_{bi}}{2},\ i = 1,2,3,4, \tag{4}$$

$$\begin{cases} \mathbf{e}_1 = \dfrac{\mathbf{x}_{m3} - \mathbf{x}_{m1}}{|\mathbf{x}_{m3} - \mathbf{x}_{m1}|}, \\ \mathbf{e}_2 = \dfrac{\mathbf{x}_{m4} - \mathbf{x}_{m2}}{|\mathbf{x}_{m4} - \mathbf{x}_{m2}|}, \end{cases} \tag{5}$$

$$\begin{cases} \mathbf{q}_1 = -\dfrac{\mathbf{e}_1 + \mathbf{e}_2}{|\mathbf{e}_1 + \mathbf{e}_2|}, \\ \mathbf{q}_2 = \dfrac{\mathbf{e}_1 - \mathbf{e}_2}{|\mathbf{e}_1 - \mathbf{e}_2|}, \\ \mathbf{q}_3 = \mathbf{q}_1 \times \mathbf{q}_2. \end{cases} \tag{6}$$

After the local coordinate system is defined (or the $\mathbf{Q}$), the separation in the local coordinate system can be calculated from Eq. (1). Different traction can be constructed with the increase of separation, like bilinear cohesive law [3], trapezoidal cohesive law [4], polynomial cohesive law [5], and exponential cohesive law [6]. Bilinear cohesive law is used to investigate artificial compliance and discontinuous force in this paper, but the proposed methods can be applied to other cohesive laws as well.

2.2 Stiffness matrix

The strain energy of a cohesive element is expressed in the local coordinate system first, as shown in Eqs. (7_1) and (7_2). This strain energy is further expressed in a global coordinate system to obtain the stiffness matrix. After the transformation to a global coordinate system, the strain energy is shown in Eq. (7_3). The relation between local traction and local separation is shown in Eqs. (8) and (9), where n, $t1$, and $t2$ mean Mode I (opening mode, normal direction), Mode II (sliding mode, tangential direction), and Mode III (tearing mode, tangential direction), respectively. Before the initiation of damage, the damage factor d is 0, and the constitutive matrix $\mathbf{C}$ is a constant matrix.

$$\begin{aligned} U &= \frac{1}{2}\iint_A (\mathbf{s}_l)^{\mathrm{T}} \boldsymbol{\sigma}_l \mathrm{d}A \\ &= \frac{1}{2}\int_A (\mathbf{s}_l)^{\mathrm{T}} \mathbf{C}\mathbf{s}_l \mathrm{d}A \\ &= \frac{1}{2}\iint_A (\mathbf{u}_t - \mathbf{u}_b)^{\mathrm{T}} \mathbf{Q}^{\mathrm{T}}\mathbf{C}\mathbf{Q}(\mathbf{u}_t - \mathbf{u}_b)\mathrm{d}A, \end{aligned} \tag{7}$$

$$\boldsymbol{\sigma}_l = \mathbf{C}\mathbf{s}_l, \tag{8}$$

$$\begin{bmatrix} \sigma_l^n \\ \tau_l^{t1} \\ \tau_l^{t2} \end{bmatrix} = \begin{bmatrix} (1-d)E_n^0 & 0 & 0 \\ 0 & (1-d)E_{t1}^0 & 0 \\ 0 & 0 & (1-d)E_{t2}^0 \end{bmatrix} \begin{bmatrix} s_l^n \\ s_l^{t1} \\ s_l^{t2} \end{bmatrix}. \tag{9}$$

Follow Eqs. (2) and (3), global displacement $\mathbf{u}_t$ and $\mathbf{u}_b$ can be expressed in terms of global displacement of nodes on top and bottom faces, as shown in Eq. (10). The summation form of global separation can be expressed into matrix form, as shown in Eq. (11). $\mathbf{N}$ is shape function matrix, $\mathbf{H}$ is the matrix mapping node displacement to global separation between top and bottom nodes, $\mathbf{d}$ is node displacement in global coordinate system, as shown in Eqs. (12)-(14), respectively. $\mathbf{H}$ is a 12 × 24 matrix. Only the first row of $\mathbf{H}$ is shown in Eq. (13) because of the size of $\mathbf{H}$, but the rest can be obtained in the same way by checking $(\mathbf{u}_t - \mathbf{u}_b)$ and $\mathbf{d}$.

$$U = \frac{1}{2}\iint_A (N_i\mathbf{u}_{ti} - N_i\mathbf{u}_{bi})^{\mathrm{T}}\mathbf{Q}^{\mathrm{T}}\mathbf{C}\mathbf{Q}(N_i\mathbf{u}_{ti} - N_i\mathbf{u}_{bi})\mathrm{d}A, \tag{10}$$

$$N_i\mathbf{u}_{ti} - N_i\mathbf{u}_{bi} = \mathbf{N}\mathbf{H}\mathbf{d}, \tag{11}$$

$$\mathbf{N} = \begin{bmatrix} N_1 & 0 & 0 & N_2 & 0 & 0 & N_3 & 0 & 0 & N_4 & 0 & 0 \\ 0 & N_1 & 0 & 0 & N_2 & 0 & 0 & N_3 & 0 & 0 & N_4 & 0 \\ 0 & 0 & N_1 & 0 & 0 & N_2 & 0 & 0 & N_3 & 0 & 0 & N_4 \end{bmatrix}, \tag{12}$$

$$\begin{aligned} \mathbf{H}(1,:) = [&1,0,0,0,0,0,0,0,0,0,0,0, \\ &-1,0,0,0,0,0,0,0,0,0,0,0], \end{aligned} \tag{13}$$

$$\begin{aligned} \mathbf{d} = [&u_{t1}, v_{t1}, w_{t1}, u_{t2}, v_{t2}, w_{t2}, u_{t3}, v_{t3}, w_{t3}, u_{t4}, v_{t4}, w_{t4}, \\ &u_{b1}, v_{b1}, w_{b1}, u_{b2}, v_{b2}, w_{b2}, u_{b3}, v_{b3}, w_{b3}, u_{b4}, v_{b4}, w_{b4}]. \end{aligned} \tag{14}$$

Put Eq. (11) into Eq. (10), strain energy is expressed as matrix form in the global coordinate system, as shown in Eq. (15), and stiffness matrix can be obtained as Eq. (16_1). Note that if the shape function matrix is expressed as $\overline{\mathbf{N}} = \mathbf{N}\mathbf{H}$, where $\overline{\mathbf{N}}$ is a 3 × 24 matrix, the stiffness matrix can be shown as Eq. (16_2). For the isoparametric element used in finite element method (FEM), $\mathrm{d}A$ is mapped into the natural coordinate system as $|\mathbf{J}|\mathrm{d}\xi\mathrm{d}\eta$, where $|\mathbf{J}|$ is the determinant of the Jacobean matrix, as shown in Eq. (17). And numerical integration can be used to calculate the stiffness matrix.

$$\begin{aligned} U &= \frac{1}{2}\iint_A \mathbf{d}^{\mathrm{T}}\mathbf{H}^{\mathrm{T}}\mathbf{N}^{\mathrm{T}}\mathbf{Q}^{\mathrm{T}}\mathbf{C}\mathbf{Q}\mathbf{N}\mathbf{H}\mathbf{d}\mathrm{d}A \\ &= \frac{1}{2}\mathbf{d}^{\mathrm{T}}\iint_A \mathbf{H}^{\mathrm{T}}\mathbf{N}^{\mathrm{T}}\mathbf{Q}^{\mathrm{T}}\mathbf{C}\mathbf{Q}\mathbf{N}\mathbf{H}\mathrm{d}A\mathbf{d}, \end{aligned} \tag{15}$$

$$\begin{aligned} K &= \iint_A \mathbf{H}^{\mathrm{T}}\mathbf{N}^{\mathrm{T}}\mathbf{Q}^{\mathrm{T}}\mathbf{C}\mathbf{Q}\mathbf{N}\mathbf{H}\mathrm{d}A \\ &= \iint_A \overline{\mathbf{N}}^{\mathrm{T}}\mathbf{Q}^{\mathrm{T}}\mathbf{C}\mathbf{Q}\overline{\mathbf{N}}\mathrm{d}A, \end{aligned} \tag{16}$$

$$K = \iint_A \mathbf{H}^{\mathrm{T}}\mathbf{N}^{\mathrm{T}}\mathbf{Q}^{\mathrm{T}}\mathbf{C}\mathbf{Q}\mathbf{N}\mathbf{H}|\mathbf{J}|\mathrm{d}\xi\mathrm{d}\eta = \iint_A \overline{\mathbf{N}}^{\mathrm{T}}\mathbf{Q}^{\mathrm{T}}\mathbf{C}\mathbf{Q}\overline{\mathbf{N}}|\mathbf{J}|\mathrm{d}\xi\mathrm{d}\eta. \tag{17}$$

The stiffness matrix presented above can be applied to a linear elastic range, but the problem becomes nonlinear after the initiation of damage when the damage factor is larger than 0 and becomes a variable. A general nonlinear equation can be solved by using the Newton-Raphson iterative method through a sequence of linearization, and an incremental procedure with a tangent stiffness matrix is needed. The general strain energy is shown in Eq. (18), where $\mathbf{u}$ is displacement, $\overline{\mathbf{u}}$ is virtual displacement, $\bar{\boldsymbol{\varepsilon}}$ is virtual strain. Linearization of this strain energy is shown in Eq. (19). Considering that incremental stress can be expressed as tangent stiffness and incremental strain, the linearization of strain energy can be further expressed as the tangent constitutive matrix, as shown in Eqs. (20) and (21). The first integrand in Eq. (21) is similar to the stiffness term in a linear system, and it is called tangent stiffness. The second integrand only happens in geometric nonlinear problems, and it is called initial stress stiffness, see Ref. [33] for detailed information.

$$U(\mathbf{u},\overline{\mathbf{u}}) = \iiint_{\Omega_0} \boldsymbol{\sigma}(\mathbf{u}) : \bar{\boldsymbol{\varepsilon}}(\mathbf{u},\overline{\mathbf{u}})\mathrm{d}\Omega, \tag{18}$$

$$L[U(\mathbf{u},\overline{\mathbf{u}})] = \iiint_{\Omega_0} (\delta\boldsymbol{\sigma} : \bar{\boldsymbol{\varepsilon}} + \boldsymbol{\sigma} : \delta\bar{\boldsymbol{\varepsilon}})\mathrm{d}\Omega, \tag{19}$$

$$\delta\boldsymbol{\sigma} = \frac{\partial\boldsymbol{\sigma}}{\partial\boldsymbol{\varepsilon}} : \delta\boldsymbol{\varepsilon} = \mathbf{C}^{\tan} : \delta\boldsymbol{\varepsilon}, \tag{20}$$

$$L[U(\mathbf{u},\overline{\mathbf{u}})] = \iiint_{\Omega_0} (\bar{\boldsymbol{\varepsilon}} : \mathbf{C}^{\tan} : \delta\boldsymbol{\varepsilon} + \boldsymbol{\sigma} : \delta\bar{\boldsymbol{\varepsilon}})\mathrm{d}\Omega. \tag{21}$$

Geometric nonlinearity of cohesive elements is not considered in this paper, and this is also taken by other papers [17,34,35]. Incremental traction is related to incremental separation through a tangent constitutive matrix as $\mathrm{d}\boldsymbol{\sigma}^1 = \mathbf{C}^{\tan}\mathrm{d}\mathbf{s}^1$, as shown in Eq. (22). To get a partial derivative of traction with respect to separation, the damage factor for bilinear cohesive law should be defined. This damage factor could be a really complicated function of local separation s_l^n, s_l^{t1}, and s_l^{t2}, see Eqs. (38)-(40) later. What is more, different failure criteria can have different δ_m^0 and δ_m^f, so the detailed expression of the damage factor is not shown here. The element in the first row and first column in $\mathbf{C}^{\tan}$ is shown in Eq. (23), and the others can be done in the same manner. After the tangent constitutive matrix is obtained, the tangent stiffness matrix can be obtained similarly, see Eq. (24).

$$\mathbf{C}^{\tan} = \begin{bmatrix} \partial\sigma_l^n/\partial s_l^n & \partial\sigma_l^n/\partial s_l^{t1} & \partial\sigma_l^n/\partial s_l^{t2} \\ \partial\tau_l^{t1}/\partial s_l^n & \partial\tau_l^{t1}/\partial s_l^{t1} & \partial\tau_l^{t1}/\partial s_l^{t2} \\ \partial\tau_l^{t2}/\partial s_l^n & \partial\tau_l^{t2}/\partial s_l^{t1} & \partial\tau_l^{t2}/\partial s_l^{t2} \end{bmatrix}, \tag{22}$$

$$\frac{\partial\sigma_l^n}{\partial s_l^n} = (1-d)E_n^0 + \left(1 - \frac{\partial d}{\partial s_l^n}\right)E_n^0 s_l^n, \tag{23}$$

$$K^{\tan} = \iint_A \mathbf{H}^{\mathrm{T}}\mathbf{N}^{\mathrm{T}}\mathbf{Q}^{\mathrm{T}}\mathbf{C}^{\tan}\mathbf{Q}\mathbf{N}\mathbf{H}\mathrm{d}A = \iint_A \overline{\mathbf{N}}^{\mathrm{T}}\mathbf{Q}^{\mathrm{T}}\mathbf{C}^{\tan}\mathbf{Q}\overline{\mathbf{N}}\mathrm{d}A. \tag{24}$$

2.3 Internal nodal force

To get the interaction between the cohesive element and bulk element, internal nodal forces should be calculated. The principle of virtual power states that the internal power equals the external power. External power can be from concentrated load, surface load, and body load, as shown in Eq. (25). However, surface force and body force are not considered in the derivation because the cohesive element used in this paper has no mass and is surrounded by solid bulk elements. The time derivative of local separation can be obtained directly from Eqs. (1) and (2), as shown in Eq. (26).

$$\iint_A (\dot{\mathbf{s}}_l)^{\mathrm{T}}\boldsymbol{\sigma}_l\mathrm{d}A = (\dot{\mathbf{x}}_{ti})^{\mathrm{T}}\mathbf{f}_{ti} + (\dot{\mathbf{x}}_{bi})^{\mathrm{T}}\mathbf{f}_{bi} + \iint_A (\dot{\mathbf{x}})^{\mathrm{T}}\mathbf{f}_S\mathrm{d}A + \iiint_V (\dot{\mathbf{x}})^{\mathrm{T}}\mathbf{f}_B\mathrm{d}V, \quad i = 1,2,3,4, \tag{25}$$

$$(\dot{\mathbf{s}}_l)^{\mathrm{T}} = \left[(\dot{\mathbf{x}}_{ti})^{\mathrm{T}}N_i(\xi,\eta) - (\dot{\mathbf{x}}_{bi})^{\mathrm{T}}N_i(\xi,\eta)\right]\mathbf{Q}^{\mathrm{T}}, \quad i = 1,2,3,4. \tag{26}$$

Substitute Eq. (26) back into Eq. (25) to get Eq. (27), and by comparing the left and right sides, internal nodal forces on the top and bottom faces can be obtained, as shown in Eq. (28).

$$\iint_A (\dot{\mathbf{s}}_l)^{\mathrm{T}}\boldsymbol{\sigma}_l\mathrm{d}A = (\dot{\mathbf{x}}_{ti})^{\mathrm{T}}\iint_A N_i(\xi,\eta)\mathbf{Q}^{\mathrm{T}}\boldsymbol{\sigma}_l\mathrm{d}A - (\dot{\mathbf{x}}_{bi})^{\mathrm{T}}\iint_A N_i(\xi,\eta)\mathbf{Q}^{\mathrm{T}}\boldsymbol{\sigma}_l\mathrm{d}A, \quad i = 1,2,3,4, \tag{27}$$

$$\begin{cases} \mathbf{f}_{ti} = \iint_A N_i(\xi,\eta)\mathbf{Q}^{\mathrm{T}}\boldsymbol{\sigma}_l\mathrm{d}A, & i = 1,2,3,4, \\ \mathbf{f}_{bi} = -\iint_A N_i(\xi,\eta)\mathbf{Q}^{\mathrm{T}}\boldsymbol{\sigma}_l\mathrm{d}A, & i = 1,2,3,4. \end{cases} \tag{28}$$

3. Artificial compliance of CZM

3.1 Analysis of artificial compliance

The first problem is artificial compliance, which increases compliance and reduces stress wave speed in dynamic problems. Stress wave speeds in 1D, 2D, and 3D solids are shown in Eq. (29). As shown in the equations, Young's modulus E, density ρ, and Poisson's ratio v are the three parameters that can alter the speed. The zero-thickness cohesive element can handle FEM modeling well, but the overall effective stiffness is implicitly decreased. To show the change caused by cohesive elements, three different types of FEM modeling are shown in Fig. 2, where blue lines and strips mean zero-thickness cohesive elements and finite-thickness cohesive elements, respectively.

$$\begin{cases} V_{1D} = \sqrt{E/\rho}\,, \\ V_{2D} = \sqrt{E/[(1-v^2)\rho]}\,, \\ V_{3D} = \sqrt{E(1-v)/[(1+v)(1-2v)\rho]}\,. \end{cases} \tag{29}$$

A 1D model of springs in series corresponding to Fig. 2 is used to explain the reason for artificial compliance, see Fig. 3. l_b and l_c are the length of bulk element and cohesive element, respectively; k_b and k_c are the stiffness of bulk element and cohesive element, respectively. The difference of finite-thickness cohesive element is that a thin layer of solid is replaced by the cohesive element, and then the deformation of the cohesive element is based on the initial material, not like zero-thickness cohesive element where its deformation is from nothing, which does not happen in reality. Parameter selection is investigated in Refs. [20,22] on stress wave speed, but cannot totally solve this problem, because zero-thickness cohesive element means extra stiffness and extra deformation.

Theoretically, the time needed for a stress wave to pass through zero-thickness cohesive elements is 0 since its length is 0, but cohesive elements would have small deformation when it is loaded, and some time is needed to pass through these deformed cohesive elements. This is the deep reason why zero-thickness cohesive elements can decrease the stress wave speed. Klein et al. [36] used a 1D example to illustrate the relation between effective stiffness and stiffness of zero-thickness cohesive element. Here, the deformation and effective stiffness corresponding to the three cases in Fig. 3 are shown in Fig. 4 and Eq. (30). For a general case with n bulk elements, the effective stiffness is shown in Eq. (31).

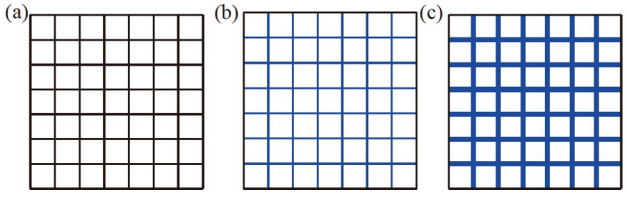

Figure 2 Different FEM modeling methods. (a) Bulk elements only; (b) bulk elements with zero-thickness cohesive elements; (c) bulk elements with finite-thickness cohesive elements.

$$\begin{cases} E_{\text{eff}} = E, & \text{bulk elements only}, \\ E_{\text{eff}}^{\text{zero}} = E\left[1 - \dfrac{1}{1+\dfrac{2l_b k_c}{E}}\right], & \text{zero-thickness}, \\ E_{\text{eff}}^{\text{finite}} = E\left[1 + \dfrac{\dfrac{l_c}{l_b} - \dfrac{E}{k_c l_b}}{2+\dfrac{E}{k_c l_b}}\right], & \text{finite-thickness}, \end{cases} \tag{30}$$

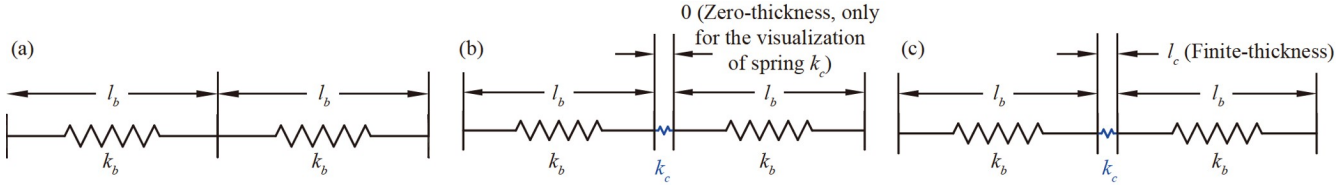

Figure 3 Different spring models. (a) Bulk elements only; (b) bulk elements with zero-thickness cohesive elements; (c) bulk elements with finite-thickness cohesive elements.

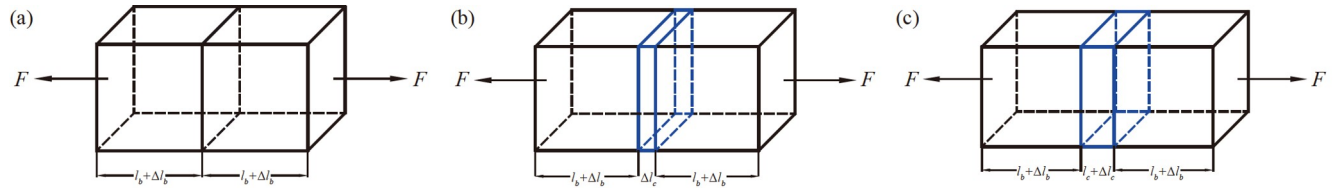

Figure 4 Deformation after load applied and illustration of artificial compliance in 1D case. (a) Bulk elements only; (b) bulk elements with zero-thickness cohesive elements; (c) bulk elements with finite-thickness cohesive elements.

$$\begin{cases} E_{\text{eff}} = E, & \text{bulk elements only,} \\ E_{\text{eff}}^{\text{zero}} = E\left[1 - \dfrac{1}{1 + \dfrac{nl_b k_c}{(n-1)E}}\right], & \text{zero-thickness,} \\ E_{\text{eff}}^{\text{finite}} = E\left[1 + \dfrac{(n-1)\dfrac{l_c}{l_b} - (n-1)\dfrac{E}{k_c l_b}}{n + \dfrac{(n-1)E}{k_c l_b}}\right], & \text{finite-thickness .} \end{cases} \tag{31}$$

For zero-thickness cohesive element, since the coefficient after Young's modulus E in Eqs. (30) and (31) is always less than 1, and its effective stiffness is always less than the stiffness of the bulk element. And this artificial compliance would be worse if a smaller bulk element (l_b) is used in the FEM model. However, a smaller element is usually required in simulations to get spatial (or grid) convergence. For a finite-thickness cohesive element, if the cohesive element stiffness k_c equals E/l_c, its effective stiffness should be equal to the stiffness of the bulk element, which means no artificial compliance. It is worth mentioning that, the expressions of stiffness for these two kinds of cohesive elements are different. For zero-thickness cohesive element, its stiffness is Young's modulus E over bulk element size l_b, while it is Young's modulus E over cohesive element size l_c (not bulk element size l_b) for finite-thickness cohesive element. After the reason for artificial compliance is explained, the finite-thickness cohesive element is proposed as an easy and effective way to solve this problem.

Artificial compliance is not only shown on stress wave speed but also on static deformation. In the rest of this Sect. 3, 1D and 3D simulations about static deformation, dynamic normal stress, and dynamic shear stress are used to explain and verify artificial compliance, and this problem is completely solved if finite-thickness cohesive element is used with proper stiffness.

3.2 Deformation in quasi-static simulation

The deformation of a bar in quasi-static conditions is investigated through MATLAB. The bar has a square cross-section, and the length of the side is 20 mm, and the total length in axial direction is 200 mm. The left end of the bar is fixed, and load is applied at the right end. The geometry, boundary condition, and load are shown in Fig. 5. The material parameters used are Young's modulus E 210 GPa, density ρ 0.00785 g/mm^3. The total number of bulk elements is 100, so the length of the bulk element l_b is 2 mm. However, for the finite-thickness cohesive elements case, the length of the bulk element l_b is 1.9 mm, and the length of the cohesive element l_c is 0.1 mm. The dynamic equation of motion is shown in Eq. (32), and the mass matrix ($\mathbf{M}_b$ and $\mathbf{M}_c$) and stiffness matrix ($\mathbf{K}_b$ and $\mathbf{K}_c$) for the three cases in Fig. 4 are shown in Eqs. (33)-(35), respectively. Note that the mass matrix for zero-thickness cohesive element is set to 0 here. r in Eqs. (34) and (35) is used to adjust the stiffness of cohesive elements.

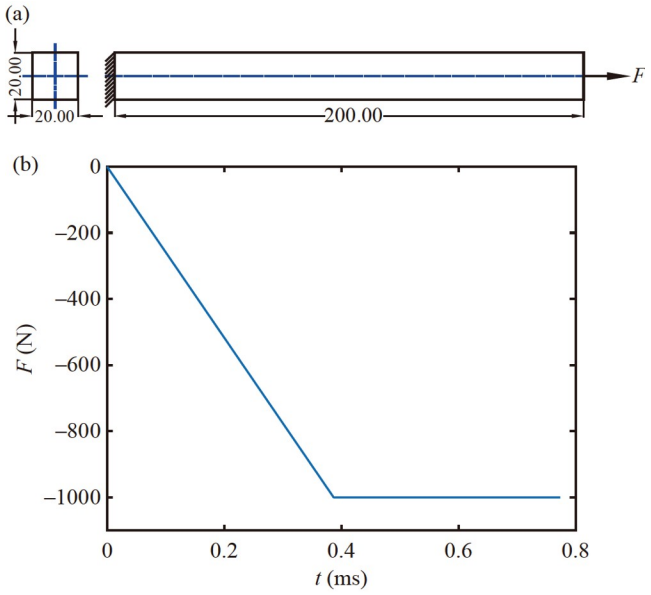

Figure 5 (a) Geometry, boundary condition, and load of the 1D bar, unit (mm); (b) detailed load at right end for the quasi-static condition.

$$[\mathbf{M}]\{\ddot{\mathbf{U}}\} + [\mathbf{C}]\{\dot{\mathbf{U}}\} + [\mathbf{K}]\{\mathbf{U}\} = \{\mathbf{F}^{\text{ext}}\}, \tag{32}$$

$$\mathbf{M}_b = \frac{\rho A l_b}{6}\begin{bmatrix} 2 & 1 \\ 1 & 2 \end{bmatrix}, \quad \mathbf{K}_b = \frac{EA}{l_b}\begin{bmatrix} 1 & -1 \\ -1 & 1 \end{bmatrix}, \tag{33}$$

$$\mathbf{M}_c^{\text{zero}} = \begin{bmatrix} 0 & 0 \\ 0 & 0 \end{bmatrix}, \quad \mathbf{K}_c^{\text{zero}} = r\frac{EA}{l_b}\begin{bmatrix} 1 & -1 \\ -1 & 1 \end{bmatrix}, \tag{34}$$

$$\mathbf{M}_c^{\text{finite}} = \frac{\rho A l_c}{6}\begin{bmatrix} 2 & 1 \\ 1 & 2 \end{bmatrix}, \quad \mathbf{K}_c^{\text{finite}} = r\frac{EA}{l_c}\begin{bmatrix} 1 & -1 \\ -1 & 1 \end{bmatrix}. \tag{35}$$

Rayleigh damping is used to construct a damping matrix to reduce oscillation and reach a steady state more quickly, as shown in Eq. (36). $\alpha 1$ and $\alpha 2$ are two coefficients to be determined from the frequency range of interest and mode damping ratio. In this paper, the interested frequency range is the frequency component that has a period equal to the time that the stress wave passes through the whole bar ω_1 and one bulk element ω_2. The two-mode damping ratios are the same and chosen as 0.1 in this paper, i.e., $\xi_1 = \xi_2 = 0.1$ in Eq. (37). Central difference method is used to solve the equation.

$$[\mathbf{C}] = \alpha 1[\mathbf{M}] + \alpha 2[\mathbf{K}], \tag{36}$$

$$0.5\begin{bmatrix} \dfrac{1}{\omega_1} & \omega_1 \\ \dfrac{1}{\omega_2} & \omega_2 \end{bmatrix}\begin{bmatrix} \alpha 1 \\ \alpha 2 \end{bmatrix} = \begin{bmatrix} \xi_1 \\ \xi_2 \end{bmatrix}. \tag{37}$$

Figure 6(a) shows the displacement at the right end of the

bar obtained for different FEM models. With the increase of r for zero-thickness cohesive element, displacement gets closer and closer to the bulk elements only case, but there is still a discrepancy between $100E/l_b$ the case and bulk elements only case. However, a finite-thickness cohesive element can have displacement totally the same as the bulk elements only case. The displacement percent error in Fig. 6(b) can show this clearly. Figure 6(c) shows the time step size scale factor needed for a successful simulation, and this scale factor decreases fast with the increase of cohesive element stiffness. We found that as long as it is less than the critical time step size, the simulation results are the same in our example. Even though the finite-thickness case has almost the same scale factor as the zero-thickness $100E/l_b$ case, the finite-thickness case can remove artificial compliance completely.

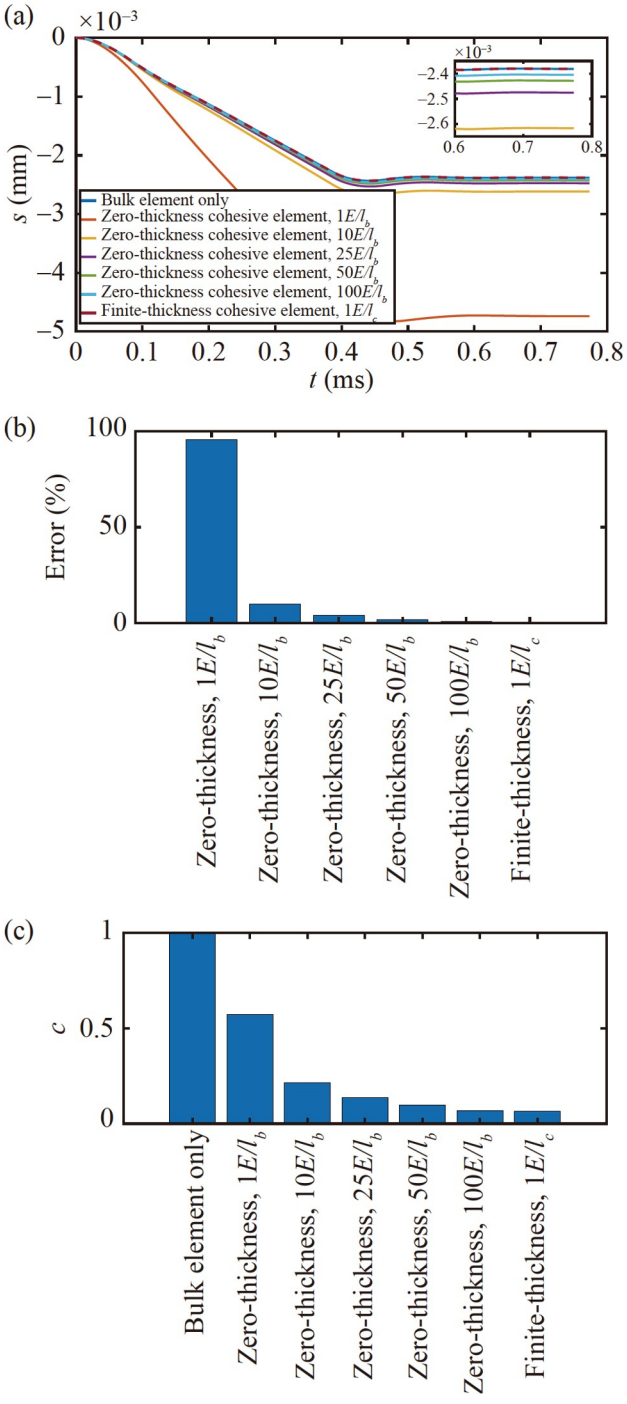

Figure 6 (a) Displacement at the right end of the bar; (b) displacement percent error; (c) time step size scale factor needed for a successful simulation.

3.3 Normal stress in dynamic simulation

Normal stress in dynamic simulation is also investigated, and 1D case in MATLAB and 3D case in LS-DYNA are presented. For the 1D case, it is almost the same as Sect. 3.1, except that load is an impact load, as shown in Fig. 7(a). The stress wave at the right end of the bar is plotted in Fig. 8. For the zero-thickness cohesive element, the stress wave is delayed even in $100E/l_b$ case, but this delay is not found for the finite-thickness cohesive element.

In the 1D case, from Eqs. (33)-(35), the zero-thickness cohesive element has similar stiffness as the bulk element, and the finite-thickness cohesive element has totally the same stiffness as the bulk element. However, in 3D case, their stiffnesses are different. In general, the bulk element has 6 stress components, but a cohesive element only deals with 3 stress components, so it is still necessary to investigate this artificial compliance in 3D case. To make a better comparison between these two types of cohesive

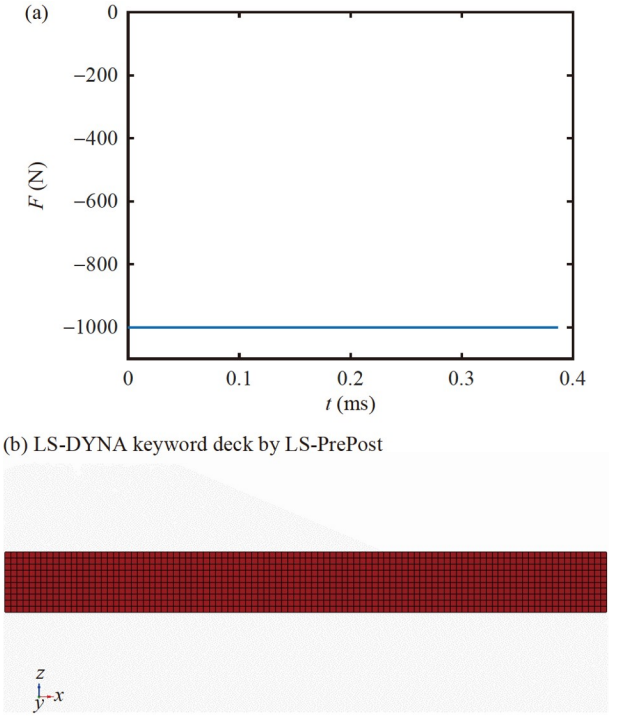

Figure 7 (a) Detailed load at right end for the dynamic condition in 1D case; (b) the bar in LS-DYNA in 3D case.

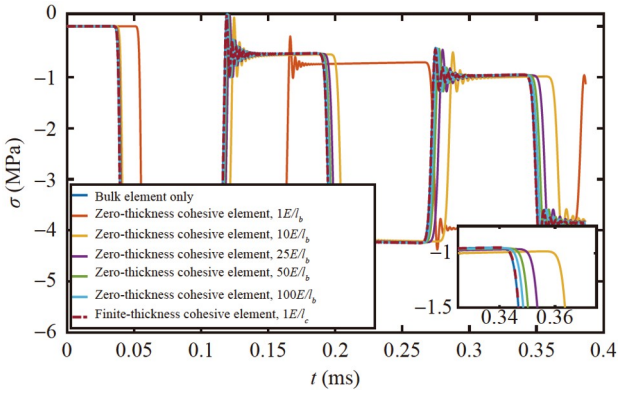

Figure 8 Stress wave at the right end of the bar in 1D case.

elements, the stiffnesses are both used as E/l_c in 3D case. The length of the bulk element l_b is 1 mm, and the length of the cohesive element l_c is 0.01 mm in the simulation, a very thin layer. For 3D case, one more parameter needed is Poisson's ratio ν 0.3. The FEM model is shown in Fig. 7(b), and the load is the same as Fig. 7(a). As shown in Fig. 9(a), the zero-thickness cohesive element cannot avoid stress wave delay even with high stiffness, but stress wave delay is removed in Fig. 9(b) with lower stiffness. The reason why stiffness in 3D case should be a little larger than the stiffness E/l_c is that Poisson's ratio ν 0.3 for bulk elements, and from V_{3D} in Eq. (29), the speed wave is faster than $\sqrt{E/\rho}$ if ν 0.3 is considered. Note that this stiffness is selected by trial and error. Even though the stiffness for a single bulk element and a single cohesive element can be obtained, the overall stiffness for a bar with many bulk elements and cohesive elements can be challenging and there might not be an analytical relation available. Stress wave speed can even be faster when a larger stiffness is used in finite-thickness cohesive element, see Fig. 9(b).

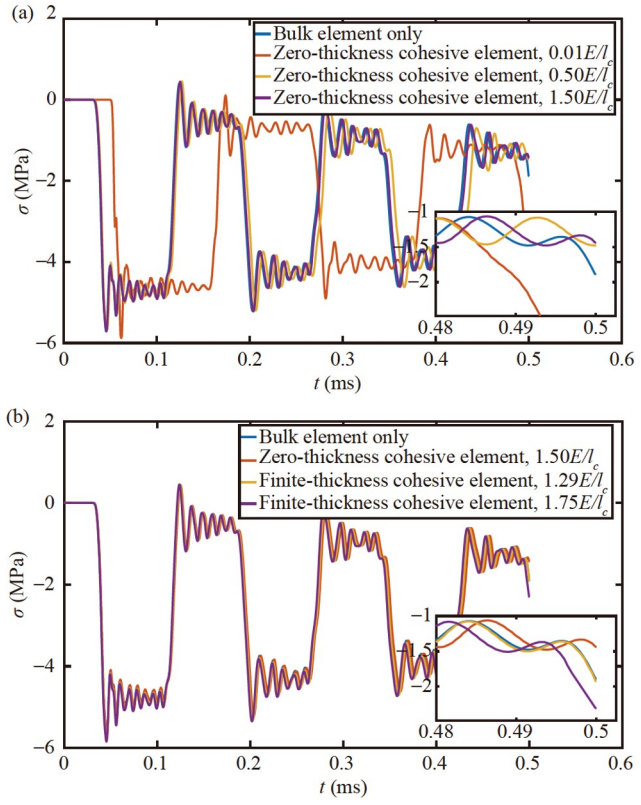

Figure 9 Stress wave at the right end of the bar for 3D case. (a) Zero-thickness cohesive element; (b) finite-thickness cohesive element.

3.4 Shear stress in dynamic simulation

Shear stress in dynamic simulation in 3D case is also investigated. The top and bottom sides of a plate with 1 mm thickness are fixed. One layer of element is used to mesh the plate, and the cube element size is 1 mm. Concentrated load is applied to the 10 nodes at the center of the left side of the plate, and the load on each node is shown in Fig. 10(b). This load is small enough that the maximum stress in the simulation is still in the elastic range. Material parameters are the same as that in Sect. 3.2. The shear stress at A randomly selected point 24.5 mm × 24.5 mm from the left bottom corner is extracted, but the same conclusion can be obtained from other positions.

The stress wave of the point is shown in Fig. 11, and

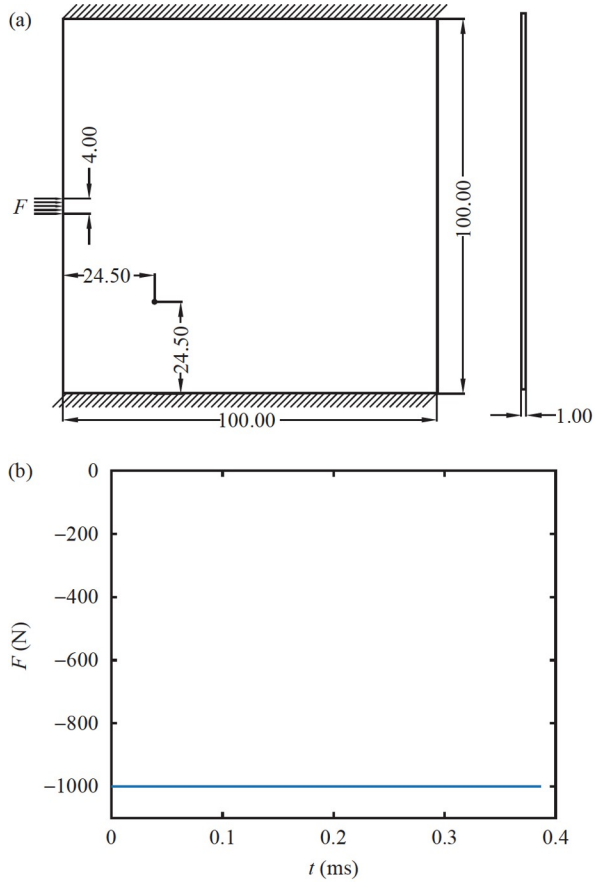

Figure 10 (a) Schematic of the plate, unit (mm); (b) concentrated load on the left side of the plate.

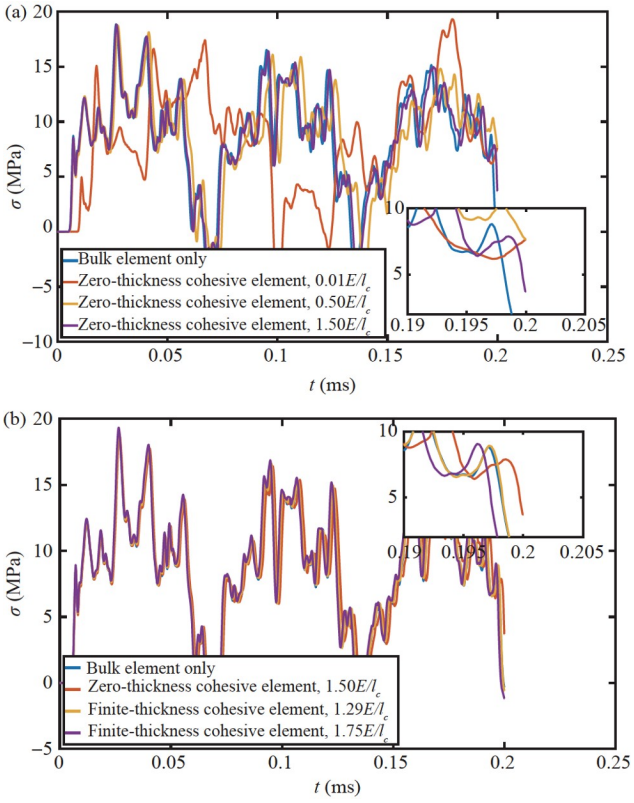

Figure 11 Stress wave of the point. (a) Zero-thickness cohesive element; (b) finite-thickness cohesive element.

similar results as normal stress cases can be found. The zero-thickness cohesive element cannot avoid stress wave delay even with high stiffness, but stress wave delay is removed in Fig. 11(b) with a lower stiffness. And stress wave speed can be even higher than bulk elements only case when a larger stiffness $1.75E/l_c$ is used. It is also found that stress wave is not correct for the zero-thickness cohesive element case when a low stiffness $0.01E/l_c$ is used in Fig. 11(a), so great caution should be taken on stiffness selection.

4. Discontinuous force of CZM

The second problem is discontinuous force. According to the authors' investigation, this discontinuous force is related to damage evolution methods. The commonly used damage evolution methods include the monotonically increasing effective separation method [27,28] and the monotonically increasing damage factor method [3,37], but both methods define the failure of the cohesive element based on whether a damage factor is larger than 1, not effective separation. For the bilinear cohesive law using quadratic stress criterion and power law, Eqs. (38) and (39) show the separations at the initiation of damage and at the failure of damage evolution, respectively.

$$\delta_m^0 = \delta_N^0 \delta_T^0 \sqrt{\frac{1+\beta^2}{\left(\beta\delta_N^0\right)^2 + \left(\delta_T^0\right)^2}}, \tag{38}$$

$$\delta_m^f = \frac{2\left(1+\beta^2\right)}{\delta_m^0}\left(\frac{E_N^0}{G_{\mathrm{IC}}^0} + \frac{\beta^2 E_T^0}{G_{\mathrm{IIC}}^0}\right)^{-1}, \tag{39}$$

where, δ_N^0 and δ_T^0 are separation at the initiation of damage in Mode I and Mode II, respectively; β is mixed mode ratio, $\sqrt{\left(s_l^{t1}\right)^2 + \left(s_l^{t2}\right)^2} / \left|s_l^n\right|$; E_N^0 and E_T^0 are stiffness in Mode I and Mode II, respectively; G_{IC}^0 and G_{IIC}^0 are critical energy release rate in Mode I and Mode II, respectively; δ_m^0 and δ_m^f are separations at the initiation of damage and at the failure of damage evolution for a mixed mode case, respectively; subscript m means mixed mode ratio. For each mixed mode ratio, there is a set of δ_m^0 and δ_m^f. The general way to calculate the damage factor is shown in Eq. (40); the reduction of stiffness because of the damage factor is shown in Eq. (41).

$$d = \begin{cases} 0, & 0 \le \Delta_m < \delta_m^0, \\ \dfrac{\delta_m^f}{\Delta_m}\left(\dfrac{\Delta_m - \delta_m^0}{\delta_m^f - \delta_m^0}\right), & \delta_m^0 \le \Delta_m < \delta_m^f, \\ 1, & \delta_m^f \le \Delta_m, \end{cases} \tag{40}$$

$$\begin{cases} E_N = (1-d)E_N^0, \\ E_T = (1-d)E_T^0, \end{cases} \tag{41}$$

where, d is damage factor; Δ_m is effective separation; E_N and E_T are the current stiffness in normal and tangential directions, respectively. Monotonically increasing effective separation and monotonically increasing damage factors are shown in Eqs. (42) and (43), respectively, but then, damage factor and effective separation can vary freely in Eqs. (42) and (43), respectively. $\Delta_{m,i}^{\mathrm{true}}$ and $d_{m,i}^{\mathrm{true}}$ are the true effective separation and true damage factor at ith time step.

$$\begin{cases} \Delta_{m,i}^{\mathrm{true}} = \max\left(\Delta_{m,[1,i-1]}^{\max}, \Delta_{m,i}\right), \\ d_{m,i}^{\mathrm{true}} = \dfrac{\delta_m^f}{\Delta_{m,i}^{\mathrm{true}}}\left(\dfrac{\Delta_{m,i}^{\mathrm{true}} - \delta_m^0}{\delta_m^f - \delta_m^0}\right), \end{cases} \tag{42}$$

$$\begin{cases} d_{m,i} = \dfrac{\delta_m^f}{\Delta_{m,i}}\left(\dfrac{\Delta_{m,i} - \delta_m^0}{\delta_m^f - \delta_m^0}\right), \\ d_{m,i}^{\mathrm{true}} = \max\left(d_{m,[1,i-1]}^{\max}, d_{m,i}\right). \end{cases} \tag{43}$$

Another thing to mention is the definition of loading, unloading, and reloading in the damage evolution process. For a loading process that has maximum history effective

separation $\Delta_{m,[1,i-1]}^{\max}$, maximum history damage factor $d_{m,[1,i-1]}^{\max}$, current effective separation $\Delta_{m,i}$, and current damage factor $d_{m,i}$, the unloading and reloading for these two methods at ith step are shown in Eqs. (44) and (45), respectively. Otherwise, it is in loading.

$$\Delta_{m,i} \le \Delta_{m,[1,i-1]}^{\max}, \tag{44}$$

$$d_{m,i} \le d_{m,[1,i-1]}^{\max}. \tag{45}$$

Since effective separation is an independent variable and damage factor is a dependent variable in Eq. (40), theoretically, another possible damage evolution method could be monotonically increasing both effective separation and damage factor method, as shown in Eq. (46). To the best of authors' knowledge, this damage evolution method has not been mentioned in other papers. In the rest of this Sect. 4, these three methods are analyzed and compared.

$$\begin{cases} \Delta_{m,i}^{\text{true}} = \max\left(\Delta_{m,[1,i-1]}^{\max}, \Delta_{m,i}\right), \\ d_{m,i} = \dfrac{\delta_m^f}{\Delta_{m,i}^{\text{true}}}\left(\dfrac{\Delta_{m,i}^{\text{true}} - \delta_m^0}{\delta_m^f - \delta_m^0}\right), \\ d_{m,i}^{\text{true}} = \max\left(d_{m,[1,i-1]}^{\max}, d_{m,i}\right). \end{cases} \tag{46}$$

4.1 Monotonically increasing effective separation, with discontinuous force

Constant unloading and reloading are an easy and straightforward method to deal with unloading and reloading, which means stiffness is a constant during the unloading and reloading process. Here, this stiffness is the same as the stiffness that happens at the maximum history effective separation or maximum history damage factor, depending on the damage evolution method used. For a monotonically increasing effective separation method, constant unloading and reloading works well for a single mixed mode ratio case, but discontinuous force can happen at the end of reloading when the mixed mode ratio changes. A single cohesive element is used to verify this, and the material parameters used are shown in Table 1.

First, two load cycles with the same mixed mode ratio are investigated, and the number of total time steps is 800. Displacement load data and mixed mode ratio range are shown in Fig. 12, where the mixed mode ratio is a constant. For the monotonically increasing effective separation method, the maximum history effective separation is shown

Table 1 Material parameters of the cohesive element

	Stiffness (MPa/mm)	Fracture strength (MPa)	Critical energy release rate (N/mm)
Mode I	100000	30	0.25
Mode II	100000	60	1.00

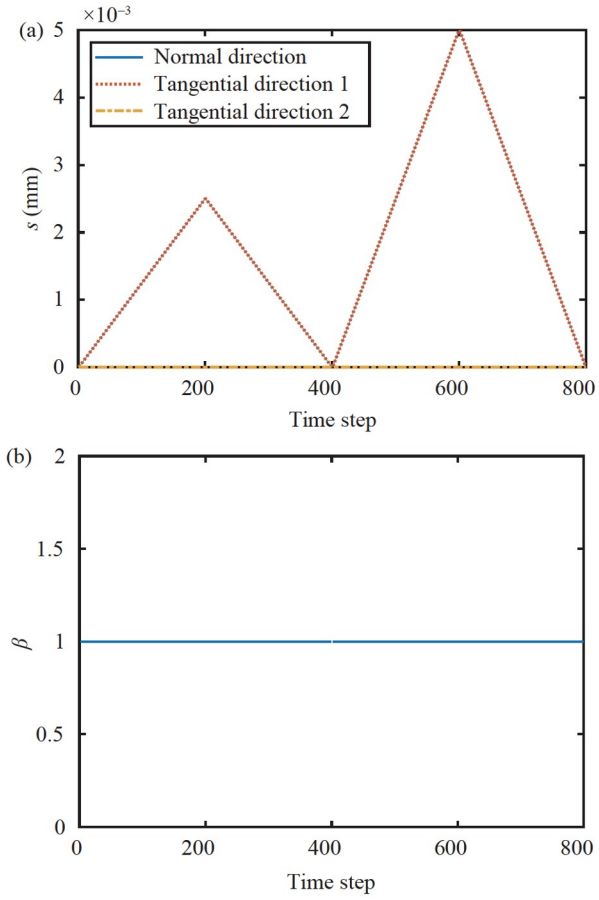

Figure 12 (a) Displacement load data; (b) mixed mode ratio range.

in Fig. 13(a), and this value keeps increasing. The damage factor is shown in Fig. 13(b). Figure 13(c) and (d) show the tangential traction response in 2D and 3D plots, respectively. As shown in these figures, discontinuous force is not found in these two cycles, and the stiffness in the unloading and reloading is constant. So, constant unloading and reloading work well for monotonically increasing effective separation methods when the mixed mode ratio does not change.

Second, two load cycles with different mixed mode ratios are investigated. Displacement load data and mixed mode ratio range are shown in Fig. 14, where the mixed mode ratio changes. For the monotonically increasing effective separation method, the maximum history effective separation is shown in Fig. 15(a), and its value is still increasing. The damage factor is shown in Fig. 15(b). Figure 15(c) and (d) show the tangential traction response in 2D and 3D plots, respectively. Discontinuous force is found in the second cycle at the end of reloading if constant unloading and reloading are used. This discontinuous force can also be seen from the damage factor in Fig. 15(b). The displacement load is continuous, but the damage factor at the end of reloading is not continuous. Or from Eqs. (38) and (39), when the mixed mode ratio β changes, δ_m^0 and δ_m^f also change, but for

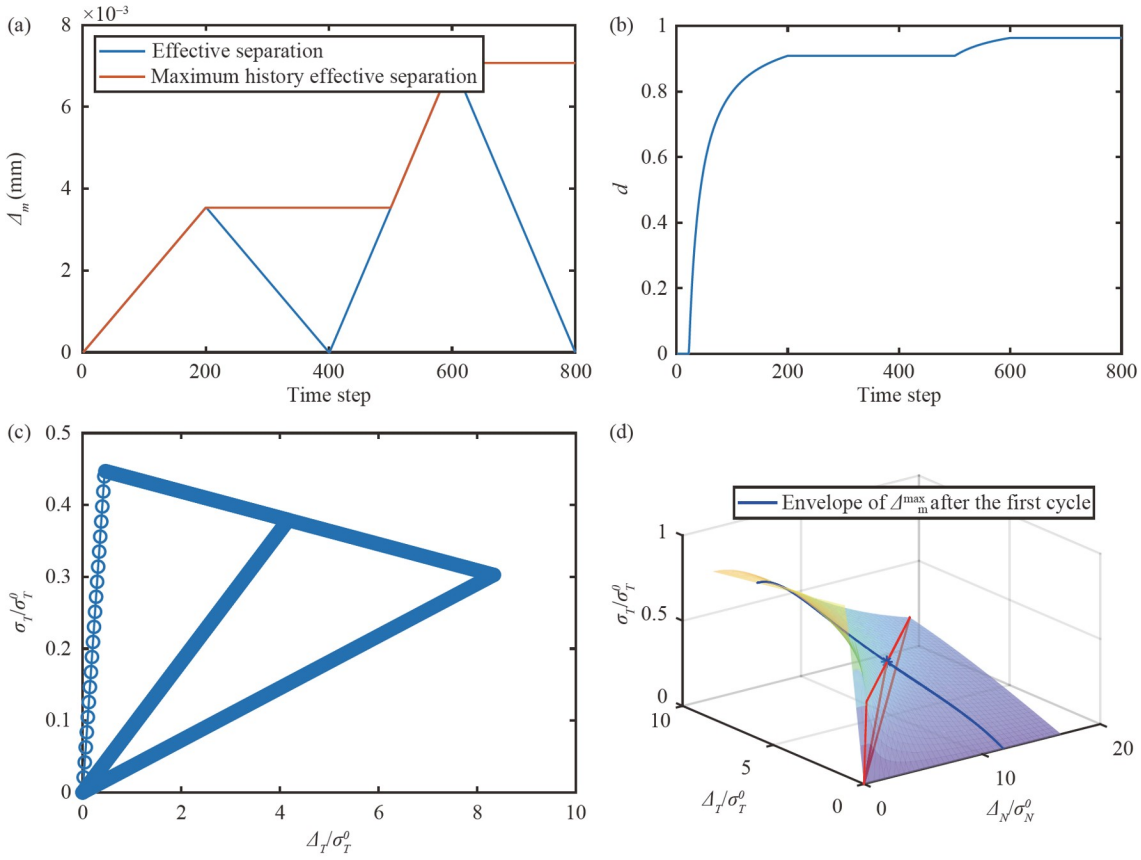

Figure 13 (a) Effective separation and maximum history effective separation; (b) damage factor; (c) tangential traction versus tangential separation; (d) tangential traction versus normal and tangential separation.

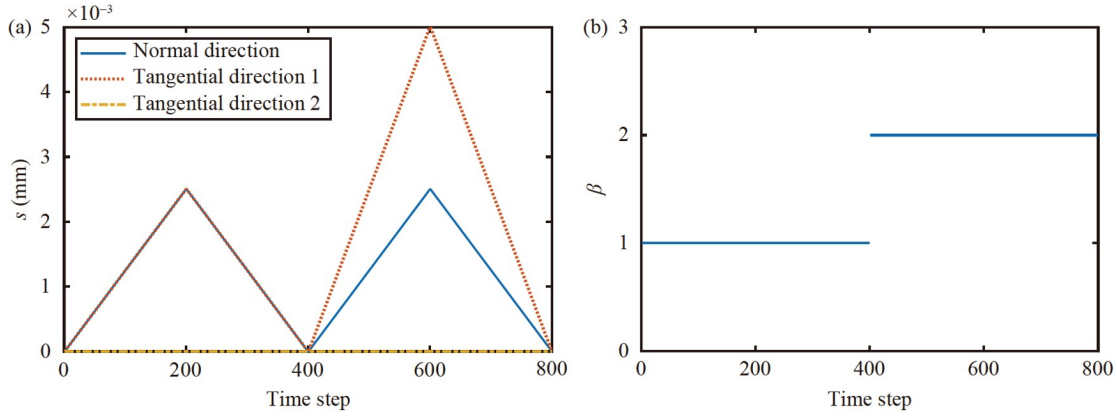

Figure 14 (a) Displacement load data; (b) mixed mode ratio range.

monotonically increasing effective separation method, maximum history effective separation is kept same at the end of reloading. From the damage factor equation in Eq. (40), it is easy to see that the stiffness of unloading in the first cycle and the stiffness of reloading in the second cycle should be different. The correct stiffness of reloading in the second cycle is shown in Fig. 15(c) and (d) with a dotted line.

A general loading process is shown in Fig. 16(a), and it has a wider range of mixed mode ratio, which changes in the whole loading process. Effective separation and damage factor are shown in Fig. 17(a) and (b), respectively. Figure 17(c) and (d) show the tangential traction response in 2D and 3D plots, respectively. As shown in these figures, discontinuous force is found in each cycle at the end of reloading, which agrees with what was found in previous simulations. The traction during loading should be exactly on the 3D cohesive law, but some tractions are above the 3D

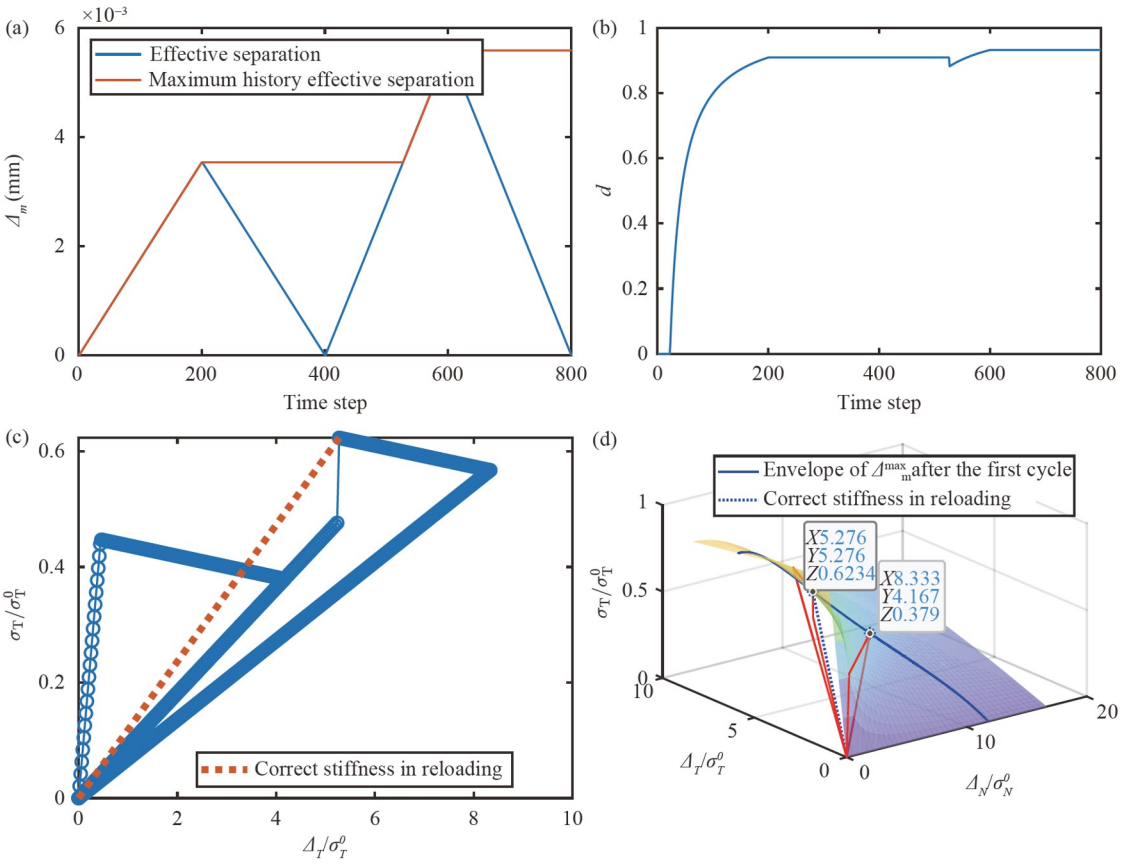

Figure 15 (a) Effective separation and maximum history effective separation; (b) damage factor; (c) tangential traction versus tangential separation; (d) tangential traction versus normal and tangential separation.

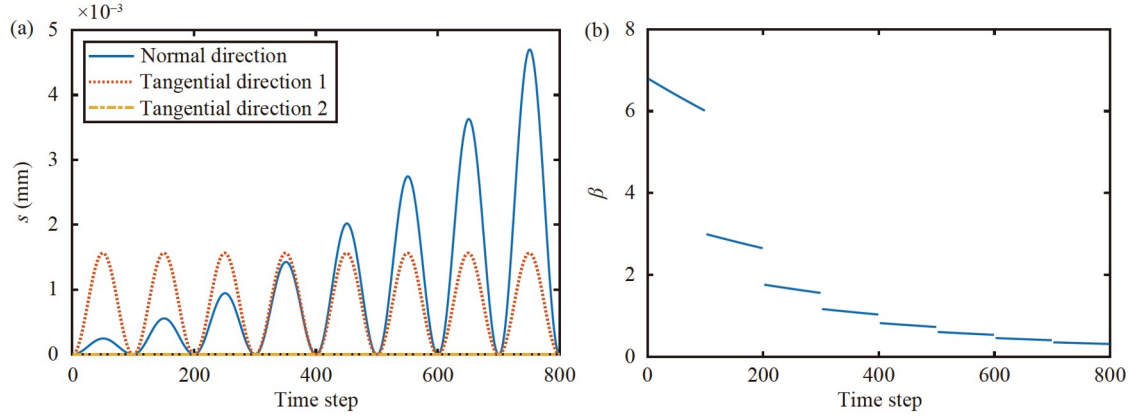

Figure 16 (a) Displacement load data; (b) mixed mode ratio range.

cohesive law in Fig. 17(d) during reloading.

4.2 Monotonically increasing effective separation, without discontinuous force

For the monotonically increasing effective separation method, a different mixed mode ratio at the same maximum history effective separation means different stiffness, and it is better to get this stiffness based on the current mixed mode ratio, not a fixed stiffness that happens at the last maximum history effective separation. Without considering plastic strain, the unloading and reloading should be on the line that connects the point on bilinear cohesive law and the origin, and then the slope (or stiffness) of this line can be calculated. Under the current mixed mode ratio, the point with maximum history effective separation is

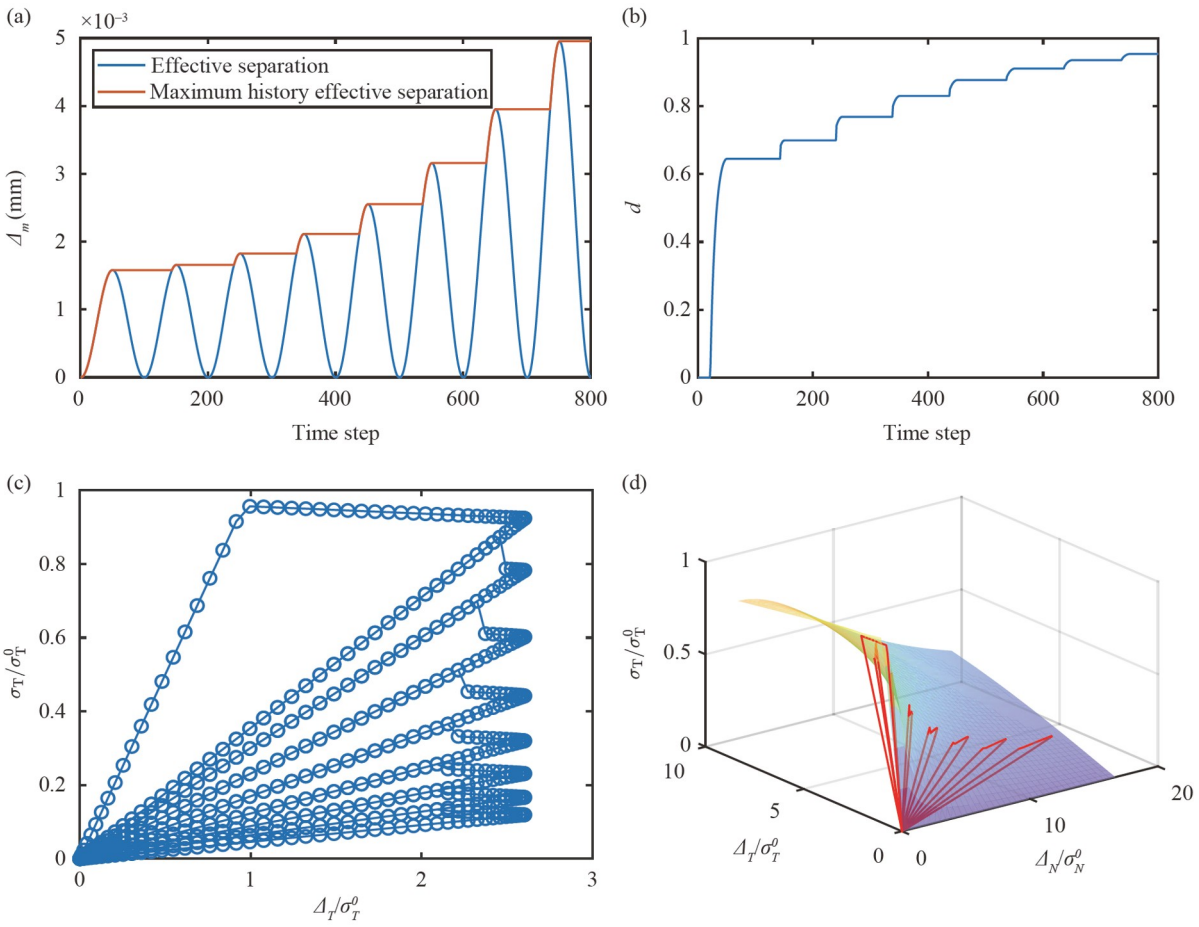

Figure 17 (a) Effective separation and maximum history effective separation; (b) damage factor; (c) tangential traction versus tangential separation; (d) tangential traction versus normal and tangential separation.

$(X, Y, Z, T_n, T_{t1}, T_{t2})$, and the point in unloading and reloading is $(x, y, z, t_n, t_{t1}, t_{t2})$, where (X, Y, Z, x, y, z) are separations and $(T_n, T_{t1}, T_{t2}, t_n, t_{t1}, t_{t2})$ are tractions in three directions. (t_n, t_{t1}, t_{t2}) is to be determined. Then linear interpolation can be used to get traction at each time step based on the current mixed mode ratio, as shown in Eq. (47).

$$\begin{cases} \sqrt{X^2+Y^2+Z^2} = \Delta_m^{\max}, \\ \dfrac{\sqrt{y^2+z^2}}{|x|} = \dfrac{\sqrt{Y^2+Z^2}}{|X|}, \\ \dfrac{x}{X} = \dfrac{t_n}{T_n}, \dfrac{y}{Y} = \dfrac{t_{t1}}{T_{t1}}, \dfrac{z}{Z} = \dfrac{t_{t2}}{T_{t2}}. \end{cases} \tag{47}$$

From Fig. 18(c) and (d), discontinuous force is not found in each cycle at the end of reloading, and the stiffness of the unloading and reloading are not the same and not constant in Fig. 18(c). However, the damage factor in Fig. 18(b) is not monotonically increasing now, which means a healing effect can happen in this method after using linear interpolation. From Sects. 4.1 and 4.2, it is easy to see that constant unloading and reloading do not work for the monotonically increasing effective separation method. The envelope of $\Delta_m^{\max}$ after the first cycle is shown in Fig. 18(d), and the point with the maximum history effective separation after the first cycle is shown in the figure. Looking downward from the top, this envelope curve is just a quarter circle with the maximum history effective separation.

4.3 Monotonically increasing damage factor, without discontinuous force

The monotonically increasing damage factor method is applied to the same displacement load. Effective separation and damage factor are shown in Fig. 19(a) and (b), respectively. Instead of the monotonically increasing effective separation, the maximum history damage factor is kept increasing, and effective separation can increase and decrease. Similarly, the point with maximum history damage factor is $(X, Y, Z, T_n, T_{t1}, T_{t2}, D)$, and the point in unloading and reloading is $(x, y, z, t_n, t_{t1}, t_{t2}, d)$, where (t_n, t_{t1}, t_{t2}) is to be determined, as shown in Eq. (48). Here, effective separation at $(X, Y, Z, T_n, T_{t1}, T_{t2}, D)$ is not required to be the maximum history effective separation. This damage evolution metho-

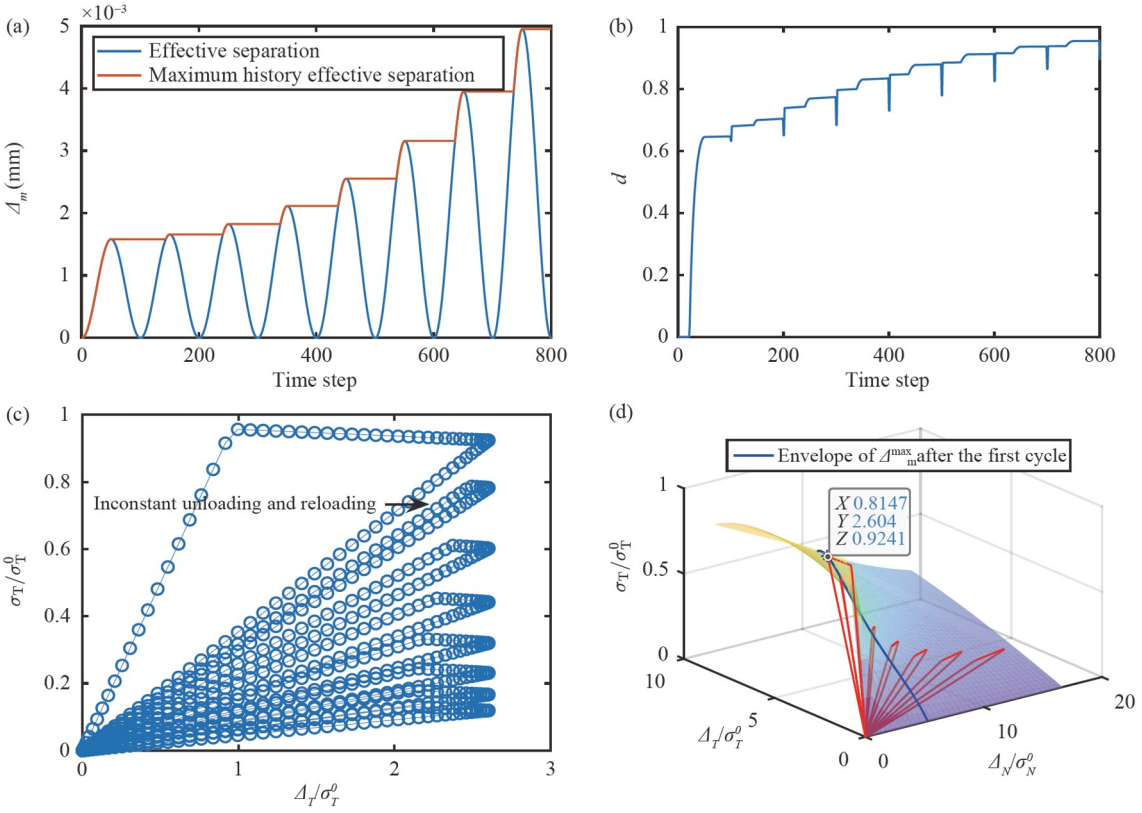

Figure 18 (a) Effective separation and maximum history effective separation; (b) damage factor; (c) tangential traction versus tangential separation; (d) tangential traction versus normal and tangential separation.

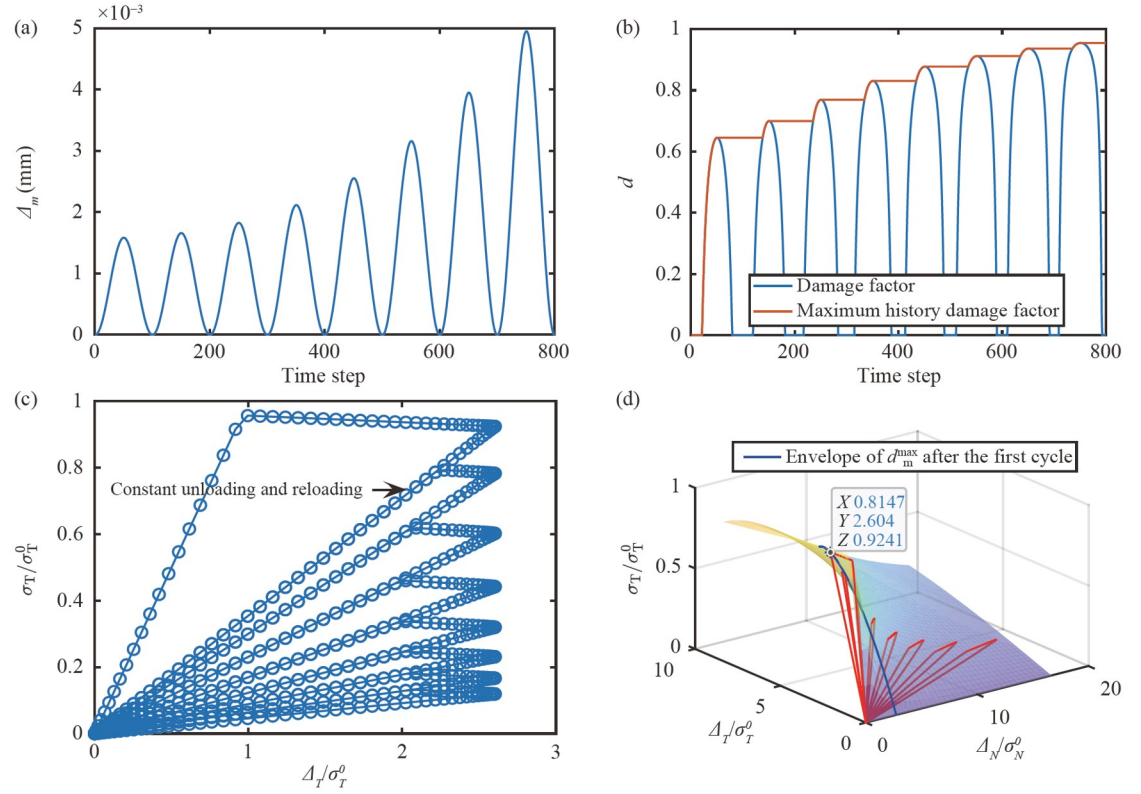

Figure 19 (a) Effective separation; (b) damage factor and maximum history damage factor; (c) tangential traction versus tangential separation; (d) tangential traction versus normal and tangential separation.

dis also used in MAT 240 in Ref. [37].

$$\begin{cases} d = D = d_m^{\max}, \\ \dfrac{\sqrt{y^2+z^2}}{|x|} = \dfrac{\sqrt{Y^2+Z^2}}{|X|}, \\ \dfrac{x}{X} = \dfrac{t_n}{T_n}, \dfrac{y}{Y} = \dfrac{t_{t1}}{T_{t1}}, \dfrac{z}{Z} = \dfrac{t_{t2}}{T_{t2}}. \end{cases} \tag{48}$$

Figure 19(c) and (d) show the tangential traction response in 2D and 3D plots, respectively. As shown in these figures, discontinuous force is not found in each cycle at the end of reloading. The big difference with the monotonically increasing effective separation method is that the stiffness of the unloading and reloading in Fig. 19(c) are the same and constant, which is because the damage evolution process is controlled by the damage factor. Before the damage factor increases, it is kept the same. In this case, constant unloading and reloading works well for the monotonically increasing damage factor method. The envelope of $d_m^{\max}$ after the first cycle is shown in Fig. 19(d), and the point with the maximum history damage factor after the first cycle is shown in the figure. Looking downward from the top, this envelope curve is a power law boundary with the maximum history damage factor.

4.4 Monotonically increasing both effective separation and damage factor, without discontinuous force

As a possible damage evolution method, monotonically increasing both effective separation and damage factor method is investigated and compared with the previous methods. From the name of this method, it has both monotonically increasing effective separation and damage factor, as shown in Eq. (49) and Fig. 20(a) and (b). Figure 20(c) and (d) show the tangential traction response in 2D and 3D plots, respectively. As shown in these figures, discontinuous force is not found in each cycle at the end of reloading. Because it has the property of monotonically increasing effective separation, the stiffnesses in unloading and reloading are not the same now. From Fig. 20(b), the damage factor is closer to 1 compared with the methods shown above. For some simulations, the damage factor could increase much faster because effective separation and damage factor are both monotonically increasing now, and caution should be taken with this method. More researches are needed to under-

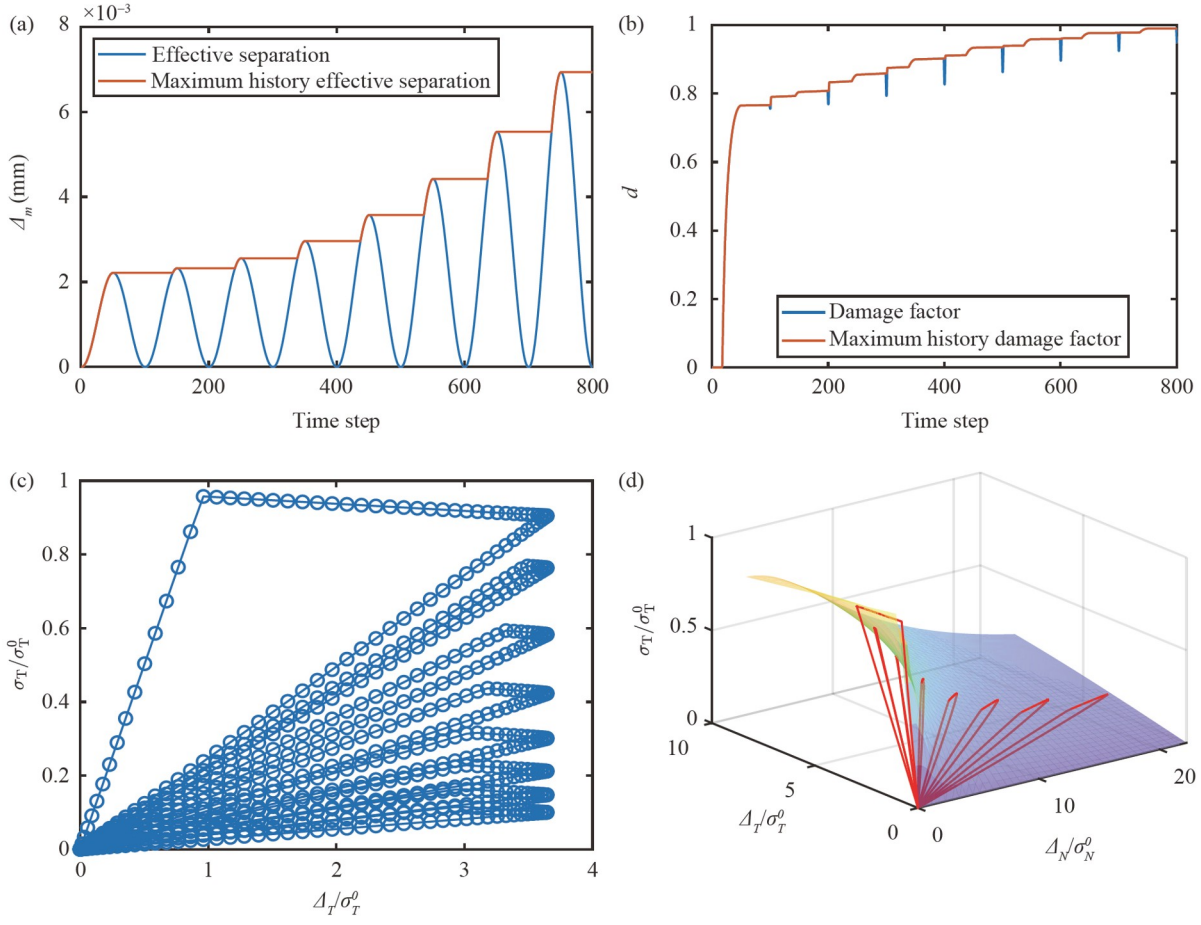

Figure 20 (a) Effective separation and maximum history effective separation; (b) damage factor and maximum history damage factor; (c) tangential traction versus tangential separation; (d) tangential traction versus normal and tangential separation.

standthe scope of its application.

$$\begin{cases} \sqrt{X^2+Y^2+Z^2} = \Delta_m^{\max}, \\ d = D = d_m^{\max}, \\ \dfrac{\sqrt{y^2+z^2}}{|x|} = \dfrac{\sqrt{Y^2+Z^2}}{|X|}, \\ \dfrac{x}{X} = \dfrac{t_n}{T_n}, \ \dfrac{y}{Y} = \dfrac{t_{t1}}{T_{t1}}, \ \dfrac{z}{Z} = \dfrac{t_{t2}}{T_{t2}}. \end{cases} \tag{49}$$

Even though the three methods work for the presented displacement load, there is still a problem with the monotonically increasing effective separation method under some special load situations, where the mixed mode ratio moves in a direction the maximum allowable separation is decreasing. For a cohesive law with δ_N^f 0.015 mm and δ_T^f 0.040 mm, different maximum history effective separation has an intersection with the power law boundary. Take the Δ_m 0.020 mm as an example, the quarter circle has an intersection with the power law boundary, and unreasonable failure would happen whenever the mixed mode ratio is at the left side of the line drawn through the origin and this intersection, because the maximum history effective separation is larger than the maximum allowable separation in that range. However, this does not happen in the monotonically increasing damage factor method where the damage evolution process is controlled by the damage factor, so there is no intersection with the power law boundary for each maximum damage factor, as shown in Fig. 21(b). In this case, no sudden failure happens just because of a change in the mixed mode ratio.

5. Numerical verifications

5.1 Artificial compliance

A drop weight tear test is used to verify the artificial compliance. A 3D rectangular pipeline steel plate has a sharp V-notch with an angle of 45° and a depth of 5 mm, as shown in Fig. 22(a). Two rigid anvils are used to support the specimen, and a rigid hammer with a mass of 40 kg and an initial velocity of 14 m/s is designed to impact the top middle of the specimen. Detailed information is shown in Ref. [38]. The pipeline steel has Young's modulus E 203 GPa, density ρ 0.00785 g/mm^3, Poisson's ratio ν 0.3. Bulk element size is 0.99 mm, and finite-thickness cohesive element size is 0.01 mm. Material parameters of the cohesive element are shown in Table 2.

Fracture crack (failed cohesive elements are deleted during simulation) and damage factor are shown in Fig. 22(b). Reaction force from the impactor and its displacement are

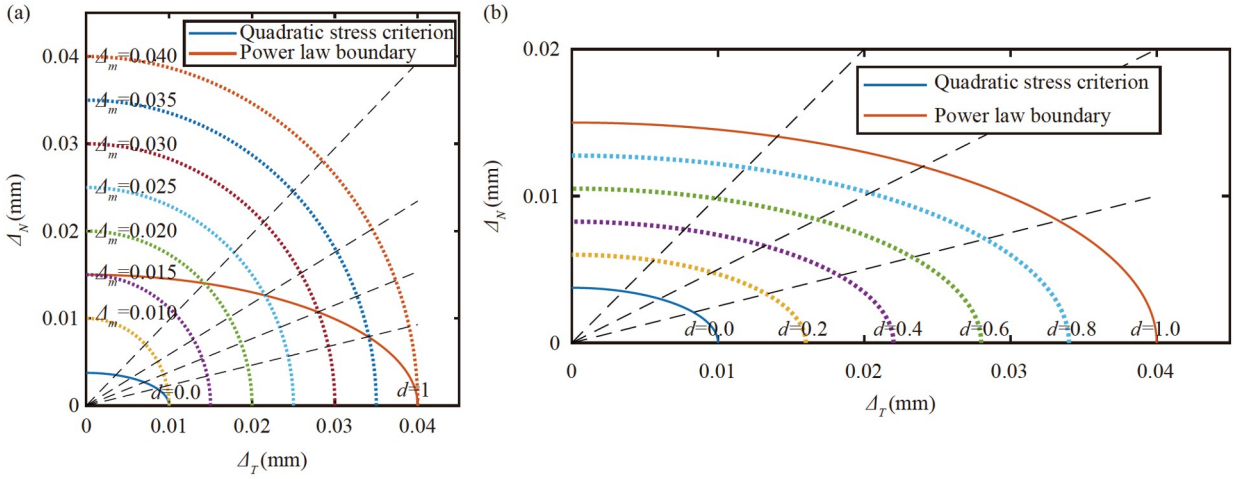

Figure 21 (a) Monotonically increasing effective separation method; (b) monotonically increasing damage factor method.

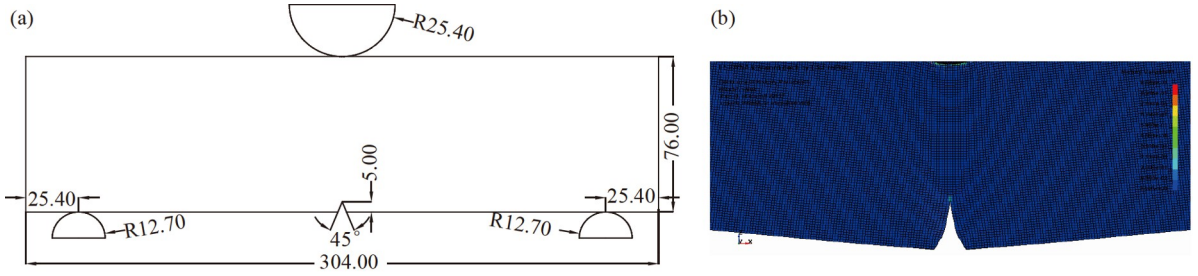

Figure 22 (a) Schematic of the plate, unit (mm); (b) fracture crack and damage factor.

Table 2 Material parameters of the cohesive element for artificial compliance analysis [38]

	Stiffness (MPa/mm)	Fracture strength (MPa)	Critical energy release rate (N/mm)
Mode I	27405000	1800	101

compared. From Fig. 23(a), the curve obtained in this paper agrees with [35] well, especially in the initial part. However, the simulation is not very close to the experiment in the initial part, and the possible reason could be the difference in boundary conditions between the experiment and the simulation. In Fig. 23(b), finite-thickness cohesive element is compared with zero-thickness cohesive element. Even though the zero-thickness cohesive element also agrees with Ref. [38], the delay of response can be seen clearly, and the delay gets bigger when time increases.

5.2 Unreasonable failure

A single cohesive element like Sect. 4 is presented here to show the unreasonable failure because of the monotonically increasing effective separation method. The material parameters of the cohesive element are shown in Table 3. From the material parameters, it can be seen that the maximum separation parameter in Mode I (0.017 mm) is less than that in Mode II (0.033 mm).

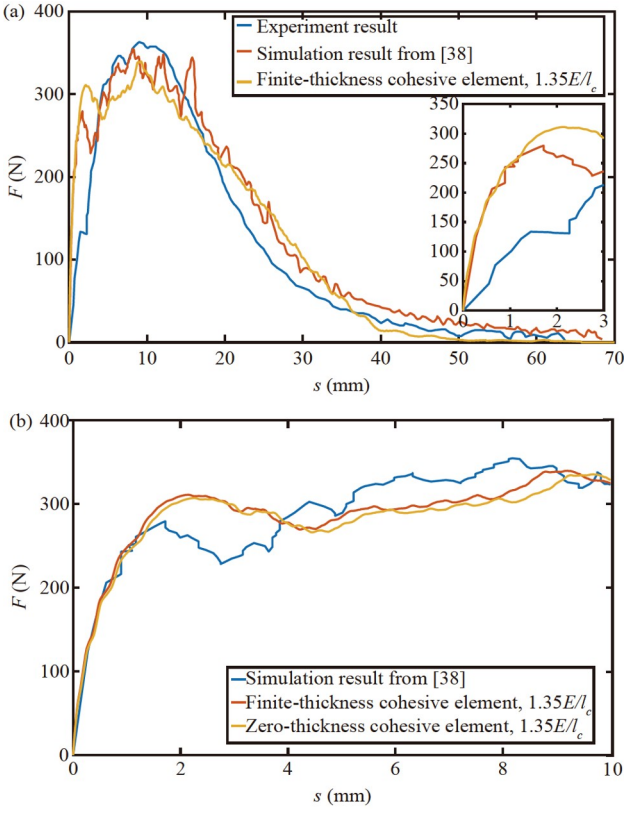

Figure 23 (a) Comparison between finite-thickness cohesive element and publications; (b) comparison between finite-thickness cohesive element and zero-thickness cohesive element.

Table 3 Material parameters of the cohesive element of unreasonable failure analysis

	Stiffness (MPa/mm)	Fracture strength (MPa)	Critical energy release rate (N/mm)
Mode I	10000	30	0.25
Mode II	10000	60	1.00

The displacement load is made that effective separation is decreasing, and the mixed mode ratio goes to the ratio that has a smaller allowable effective separation, which is closer to pure normal load in this case, as shown in Fig. 24(a) and (b). The maximum history effective separation and the change of damage factor are shown in Fig. 24(c) and (d), respectively. The same thing, the healing effect is found in Fig. 24(d) in this method, which is not what we want.

From the damage factor, it can be seen that at the end of the 7th cycle, the damage factor is 0.9942, but just at the start of the 8th cycle, the damage factor becomes 1 even though the displacement load at the start of the 8th cycle is just 0. This can also be explained from the top view of cohesive law. The maximum history effective separation in Fig. 25(a) has an intersection with the power law boundary, and if the displacement load goes above the purple line, the cohesive element would fail immediately, which could be unreasonable for some situations. Another special loading condition is a tangential load followed by a normal load, where the change of mixed mode ratio is maximum, but this failure because of the only change of load direction may not agree with the experiment.

6. Conclusions

In this paper, artificial compliance and discontinuous force in CZM are investigated. Different FEM modeling methods and different damage evolution methods are analyzed to solve the two problems. Several 1D and 3D simulations have been conducted to verify the improvements proposed. The conclusions obtained are shown as follows:

(1) Zero-thickness cohesive element and finite-thickness cohesive element are compared.

(a) The reason for artificial compliance in zero-thickness cohesive element is its extra stiffness and extra deformation. The zero-thickness cohesive element cannot remove artificial compliance by just using higher stiffness. Effective stiffness for zero-thickness cohesive elements and finite-thickness cohesive elements are different. For the zero-thickness cohesive element, it is bulk modulus E over the size of a bulk element l_b, whereas, for a finite-thickness cohesive element, it is bulk modulus E over the size of the cohesive element l_c.

(b) For those time-sensitive simulations with long simulation time, the finite-thickness cohesive element could be

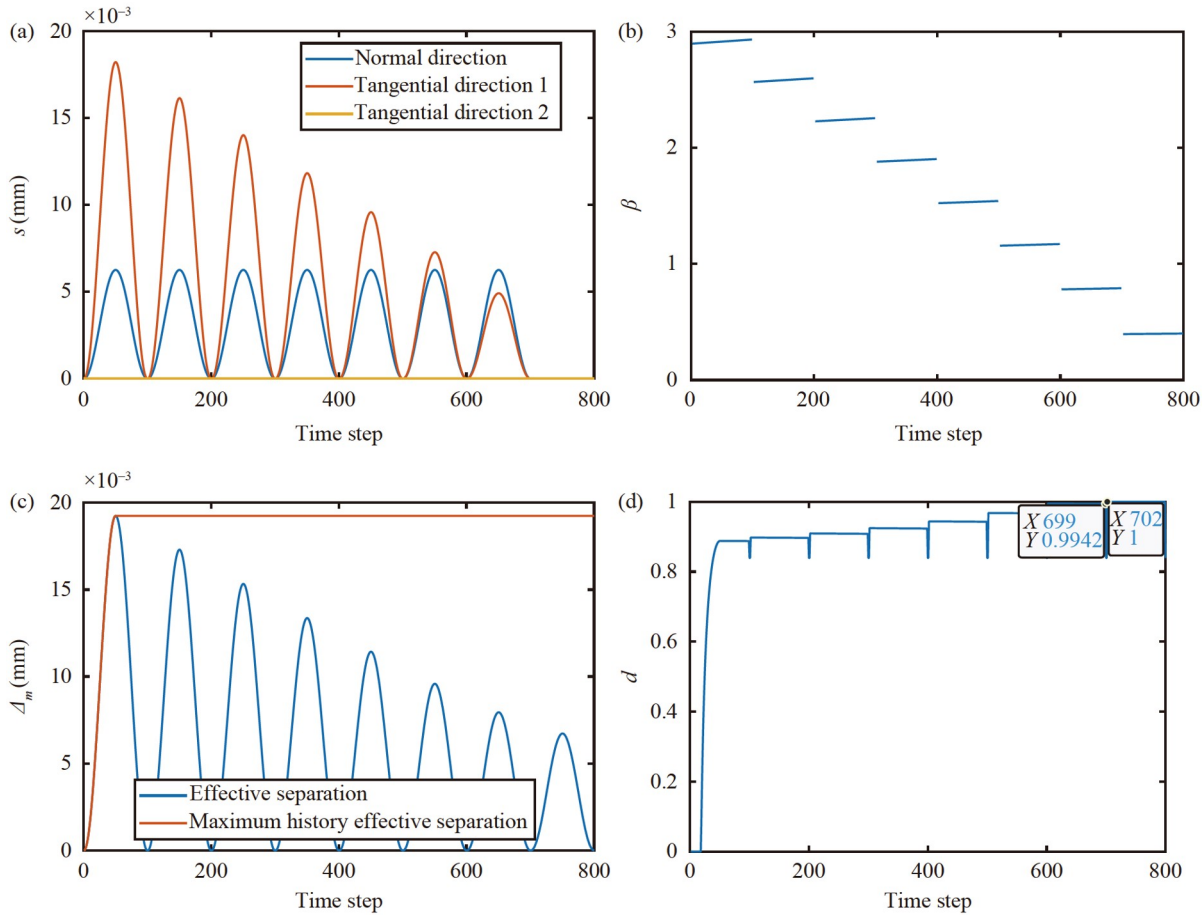

Figure 24 (a) Displacement load data; (b) mixed mode ratio range; (c) effective separation and maximum history effective separation; (d) damage factor.

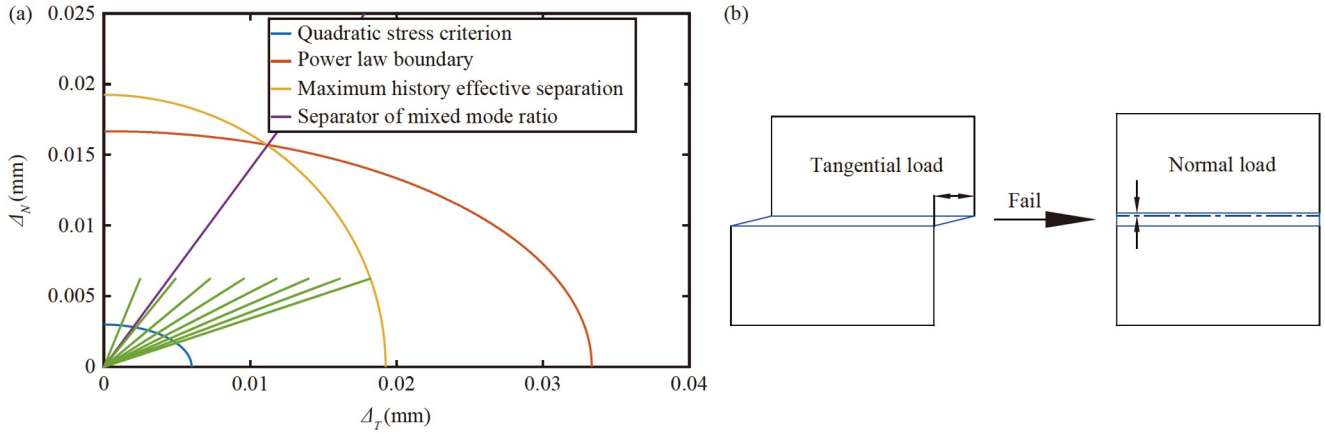

Figure 25 (a) Explanation of the unreasonable failure in monotonically increasing effective separation method; (b) unreasonable failure in a special loading condition.

an easy and numerically efficient way to remove artificial compliance by using proper stiffness parameters.

(2) Three damage evolution methods (monotonically increasing effective separation, damage factor, and both effective separation and damage factor) are analyzed and compared.

(a) Discontinuous force happens when the monotonically increasing effective separation method is used with constant unloading and reloading. Linear interpellation based on the current mixed mode ratio can be used to solve this discontinuous force. Monotonically increasing effective separation method can lead to unreasonable failure when maximum separation parameters in Mode I and Mode II are different.

(b) The monotonically increasing damage factor method has the inherent property to enable constant unloading and reloading in the damage evolution process, and no unreasonable failure, which is a better choice compared with the other two methods.

Conflict of interest *On behalf of all authors, the corresponding author states that there is no conflict of interest.*

Author contributions ***Ala Tabiei****: Software, Data curation, Resources, Writing – review and editing, Supervision, Project administration.* ***Li Meng****: Conceptualization, Methodology, Investigation, Software, Data curation, Validation, Writing – original draft, Writing – review and editing.*

1 G. I. Barenblatt, The formation of equilibrium cracks during brittle fracture. General ideas and hypotheses. Axially-symmetric cracks, J. Appl. Math. Mech. **23**, 622 (1959).
2 D. S. Dugdale, Yielding of steel sheets containing slits, J. Mech. Phys. Solids **8**, 100 (1960).
3 L. Meng, and A. Tabiei, An irreversible bilinear cohesive law considering the effects of strain rate and plastic strain and enabling reciprocating load, Eng. Fract. Mech. **252**, 107855 (2021).
4 M. May, O. Hesebeck, S. Marzi, W. Böhme, J. Lienhard, S. Kilchert, M. Brede, and S. Hiermaier, Rate dependent behavior of crash-optimized adhesives — Experimental characterization, model development, and simulation, Eng. Fract. Mech. **133**, 112 (2015).
5 Y. Freed, and L. Banks-Sills, A new cohesive zone model for mixed mode interface fracture in bimaterials, Eng. Fract. Mech. **75**, 4583 (2008).
6 P. F. Liu, and M. M. Islam, A nonlinear cohesive model for mixed-mode delamination of composite laminates, Compos. Struct. **106**, 47 (2013).
7 S. Abrate, J. F. Ferrero, and P. Navarro, Cohesive zone models and impact damage predictions for composite structures, Meccanica **50**, 2587 (2015).
8 N. V. De Carvalho, M. W. Czabaj, and J. G. Ratcliffe, Piecewise-linear generalizable cohesive element approach for simulating mixed-mode delamination, Eng. Fract. Mech. **242**, 107484 (2021).
9 M. F. S. F. de Moura, J. P. M. Gonçalves, and F. G. A. Silva, A new energy based mixed-mode cohesive zone model, Int. J. Solids Struct. **102-103**, 112 (2016).
10 T. Yamaguchi, T. Okabe, and S. Yashiro, Fatigue simulation for titanium/CFRP hybrid laminates using cohesive elements, Compos. Sci. Tech. **69**, 1968 (2009).
11 D. Kumar, R. Roy, J. H. Kweon, and J. Choi, Numerical modeling of combined matrix cracking and delamination in composite laminates using cohesive elements, Appl. Compos. Mater. **23**, 397 (2016).
12 C. Sarrado, F. A. Leone, and A. Turon, Finite-thickness cohesive elements for modeling thick adhesives, Eng. Fract. Mech. **168**, 105 (2016).
13 W. Trawiński, J. Bobiński, and J. Tejchman, Two-dimensional simulations of concrete fracture at aggregate level with cohesive elements based on X-ray μCT images, Eng. Fract. Mech. **168**, 204 (2016).
14 W. Trawiński, J. Tejchman, and J. Bobiński, A three-dimensional meso-scale modelling of concrete fracture, based on cohesive elements and X-ray μCT images, Eng. Fract. Mech. **189**, 27 (2018).
15 K. Park, and G. H. Paulino, Computational implementation of the PPR potential-based cohesive model in ABAQUS: Educational perspective, Eng. Fract. Mech. **93**, 239 (2012).
16 P. Rahul-Kumar, A. Jagota, S. J. Bennison, S. Saigal, and S. Muralidhar, Polymer interfacial fracture simulations using cohesive elements, Acta Mater. **47**, 4161 (1999).
17 B. L. V. Bak, E. Lindgaard, and E. Lund, Analysis of the integration of cohesive elements in regard to utilization of coarse mesh in laminated composite materials, Numer. Meth. Eng. **99**, 566 (2014).
18 A. Tabiei, and L. Meng, Improved cohesive zone model: Integrating strain rate, plastic strain, variable damping, and enhanced constitutive law for fracture propagation, Int. J. Fract **244**, 125 (2023).
19 S. H. Song, G. H. Paulino, and W. G. Buttlar, A bilinear cohesive zone model tailored for fracture of asphalt concrete considering viscoelastic bulk material, Eng. Fract. Mech. **73**, 2829 (2006).
20 N. Blal, L. Daridon, Y. Monerie, and S. Pagano, Micromechanical-based criteria for the calibration of cohesive zone parameters, J. Comput. Appl. Math. **246**, 206 (2013).
21 V. P. Nguyen, Discontinuous Galerkin/extrinsic cohesive zone modeling: Implementation caveats and applications in computational fracture mechanics, Eng. Fract. Mech. **128**, 37 (2014).
22 A. Tabiei, and W. Zhang, Cohesive element approach for dynamic crack propagation: Artificial compliance and mesh dependency, Eng. Fract. Mech. **180**, 23 (2017).
23 W. Zhang, and A. Tabiei, Improvement of an exponential cohesive zone model for fatigue analysis, J. Fail. Anal. Preven. **18**, 607 (2018).
24 V. Tomar, J. Zhai, and M. Zhou, Bounds for element size in a variable stiffness cohesive finite element model, Numer. Meth. Eng. **61**, 1894 (2004).
25 S. Kozinov, M. Kuna, and S. Roth, A cohesive zone model for the electromechanical damage of piezoelectric/ferroelectric materials, Smart Mater. Struct. **23**, 055024 (2014).
26 K. Park, and G. H. Paulino, Cohesive zone models: A critical review of traction-separation relationships across fracture surfaces, Appl. Mech. Rev. **64**, 060802 (2011).
27 W. Gao, J. Xiang, S. Chen, S. Yin, M. Zang, and X. Zheng, Intrinsic cohesive modeling of impact fracture behavior of laminated glass, Mater. Des. **127**, 321 (2017).
28 F. Hirsch, and M. Kästner, Microscale simulation of adhesive and cohesive failure in rough interfaces, Eng. Fract. Mech. **178**, 416 (2017).
29 A. Turon, P. P. Camanho, J. Costa, and J. Renart, Accurate simulation of delamination growth under mixed-mode loading using cohesive elements: Definition of interlaminar strengths and elastic stiffness, Compos. Struct. **92**, 1857 (2010).
30 C. Sarrado, A. Turon, J. Renart, and I. Urresti, Assessment of energy dissipation during mixed-mode delamination growth using cohesive zone models, Compos. Part A-Appl. Sci. Manufact. **43**, 2128 (2012).
31 A. Turon, E. V. González, C. Sarrado, G. Guillamet, and P. Maimí, Accurate simulation of delamination under mixed-mode loading using a cohesive model with a mode-dependent penalty stiffness, Compos. Struct. **184**, 506 (2018).
32 L. A. de Oliveira, and M. V. Donadon, Delamination analysis using cohesive zone model: A discussion on traction-separation law and mixed-mode criteria, Eng. Fract. Mech. **228**, 106922 (2020).
33 N. H. Kim, Introduction to Nonlinear Finite Element Analysis (Springer, New York, 2014).
34 P. Rahulkumar, A. Jagota, S. J. Bennison, and S. Saigal, Cohesive element modeling of viscoelastic fracture: Application to peel testing of polymers, Int. J. Solids Struct. **37**, 1873 (2000).
35 D. W. Spring, and G. H. Paulino, A growing library of three-dimensional cohesive elements for use in ABAQUS, Eng. Fract. Mech. **126**, 190 (2014).
36 P. A. Klein, J. W. Foulk, E. P. Chen, S. A. Wimmer, and H. J. Gao, Physics-based modeling of brittle fracture: Cohesive formulations and the application of meshfree methods, Theor. Appl. Fract. Mech. **37**, 99 (2001).
37 Livermore Software Technology Corporation, LS-DYNA Keyword User's Manual, Vol. II Material Models (LSTC, Livermore, 2019).
38 Z. J. Ren, and C. Q. Ru, Numerical investigation of speed dependent

dynamic fracture toughness of line pipe steels, Eng. Fract. Mech. **99**, 214 (2013).

黏结区模型在人工柔度和不连续力方面的改进

Ala Tabiei, 孟礼

摘要 黏结区模型在断裂扩展方面被广泛而成功的应用, 但仍然存在一些基本问题被忽视需要解决. 本文研究了黏结区模型中的人工柔度和不连续力. 首先, 介绍了关于黏结单元(局部坐标系、刚度矩阵和内部节点力)的理论. 局部坐标系被定义用于获得局部分离. 八节点黏结单元的刚度矩阵是从应变能的计算中导出的. 黏结单元与体积单元之间的内部节点力是根据虚功原理得出的. 其次, 从零厚度和有限厚度的黏结单元的有效刚度角度解释了人工柔度的原因. 基于有限厚度黏结单元的有效刚度, 可以通过调整黏结单元的刚度来完全消除人工柔度. 1D和3D模拟验证了这一结论. 第三, 分析了三种损伤演化方法(单调增加的有效分离、损伤因子以及有效分离和损伤因子的结合). 在恒定卸载和重新加载条件下, 没有不连续力和愈合效应的单调增加的损伤因子方法显示出比其他两种方法更好的选择. 所提出的改进方法已经编码到LS-DYNA用户定义材料中, 并且通过落锤撕裂试验获得的模拟结果验证了这些改进.